

RAIM Detector and Estimator Design to Minimize the Integrity Risk

Mathieu Joerger, Fang-Cheng Chan, Steven Langel, and Boris Pervan
Illinois Institute of Technology

BIOGRAPHY

Dr. Mathieu Joerger obtained a Master in Mechatronics from the National Institute of Applied Sciences in Strasbourg, France, in 2002, and a M.S. and a Ph.D. in Mechanical and Aerospace Engineering from the Illinois Institute of Technology (IIT), in 2002 and 2009 respectively. He is the 2009 recipient of the Institute of Navigation (ION) Bradford Parkinson award, which honors outstanding graduate students in the field of GNSS. Mathieu is currently a research assistant professor at IIT, working on multi-sensor integration, on sequential fault-detection for multi-constellation navigation systems, and on differential and relative receiver autonomous integrity monitoring (RAIM) for shipboard landing of military aircraft.

Fang-Cheng Chan is a Senior Research Associate at Navigation Laboratory in the Department of Mechanical and Aerospace Engineering at IIT in Chicago. He received his Ph.D in mechanical and aerospace engineering from IIT, Chicago, in 2008. He is currently working on GPS receiver integrity for Local Area Augmentation System (LAAS) ground receivers, and developing navigation and fault detection algorithms for Technical Subgroup of EU/US Working Group C (WGC) with focus on RAIM. Dr. Chan is a member of American Institute of Aeronautics and Astronautics, and a member of ION.

Steven Langel is a PhD candidate at IIT whose work focuses on the design of high accuracy, high integrity navigation algorithms for aerospace applications. Specific research interests include carrier phase differential GPS navigation with cycle resolution, Kalman filtering with stochastic modeling uncertainty and the design of GPS / INS integration algorithms. Steven received his B.S. degree in mechanical and aerospace engineering from IIT.

Dr. Boris Pervan is Professor of Mechanical and Aerospace Engineering at IIT, where he conducts research on high-integrity satellite navigation systems. Prof. Pervan received his B.S. from the University of Notre Dame, M.S. from the California Institute of Technology, and Ph.D. from Stanford University. Prior to joining the

faculty at IIT, he was a spacecraft mission analyst at Hughes Space and Communications Group and was project leader at Stanford University for GPS LAAS research and development. He was the recipient of the Mechanical and Aerospace Dept. Excellence in Research Award (2007), IIT/Sigma Xi Excellence in University Research Award (2005), University Excellence in Teaching Award (2005), Ralph Barnett Mechanical and Aerospace Dept. Outstanding Teaching Award (2002, 2009), IEEE Aerospace and Electronic Systems Society M. Barry Carlton Award (1999), RTCA William E. Jackson Award (1996), Guggenheim Fellowship (Caltech 1987), and Albert J. Zahm Prize in Aeronautics (Notre Dame 1986). He is currently Editor of the ION journal Navigation.

ABSTRACT

Future multi-constellation GNSS open the possibility to fulfill stringent navigation integrity requirements specified in safety-critical applications using receiver autonomous integrity monitoring (RAIM). In this paper, both the RAIM detector and its estimator are analyzed to develop a new algorithm. In the first part of this paper, the detector is selected by rigorously comparing two of the most widely implemented methods. In particular, the paper reveals fundamental differences between solution separation (SS) and residual-based (RB) RAIM. SS provides higher fault-detection performance than RB RAIM because the SS test statistic is tailored to the fault hypothesis, and to the state of interest. To prove these results in presence of multi-measurement faults, which occur in multi-constellation GNSS, analytical expressions of the worst-case fault direction are derived for both SS and RB RAIM. In the second part of the paper, a non-least-squares estimator is designed to reduce the integrity risk at the cost of lower accuracy performance for applications where integrity requirements are more demanding than accuracy requirements. The new estimator is numerically determined by solving an integrity risk minimization problem that includes multiple simultaneous fault hypotheses. Performance analyses show a substantial drop in integrity risk using the new

RAIM algorithm as compared to a SS method that uses a least-squares estimator. In parallel, the decrease in accuracy performance is quantified. Combined availability of accuracy and integrity is evaluated at an example location for a GPS/Galileo navigation system.

I. INTRODUCTION

This paper describes the design, analysis and evaluation of a new method of receiver autonomous integrity monitoring (RAIM). Both the detector and the estimator used in RAIM are investigated in order to minimize the integrity risk in the presence of multiple simultaneous measurement faults.

Global navigation satellite system (GNSS) measurements are vulnerable to rare-event faults such as satellite failures. In safety-critical applications, these faults can represent major threats to the navigation system's integrity. In response, fault-detection algorithms such as RAIM can be implemented. RAIM achieves self-contained fault detection at the user receiver by verifying the consistency of the over-determined positioning solution using redundant ranging measurements.

The full deployment of GLONASS and the emergence of Galileo will provide an increased number of redundant ranging signals, which has recently motivated a renewed interest in RAIM. In particular, RAIM can help alleviate requirements on ground monitors used in safety critical applications. For example, researchers in the European Union and in the United States are investigating Advanced RAIM (ARAIM) for worldwide vertical guidance of aircraft [1]. Challenges arise when using multi-constellation GNSS because of the substantial increase in the probability of multiple simultaneous faults, which must hence be detected.

In addition, RAIM not only aims at detecting faults but also at evaluating the integrity risk, or alternatively, a protection level, which is an integrity-bound on the position estimate error. In practice, integrity risk evaluation is needed when designing navigation systems to meet required levels of integrity, and it is needed operationally to predict if a mission can be safely initiated. Integrity risk evaluation includes both assessing the fault detection capability and quantifying the impact of undetected faults on state estimate errors. Hence, both the detector and the estimator can influence RAIM performance.

One more point worth noticing is that integrity risk evaluation is based upon a model of the measurements. In contrast with nominal measurement errors, whose distributions can be reliably modeled using large amounts of experimental data, measurement faults are difficult to observe because of their low probability of occurrence. In

order to avoid making assumptions on unknown fault distributions, a bound on the integrity risk corresponding to the worst-case fault can be evaluated. This bound is then compared to a specified integrity risk requirement to assess availability, which is defined as the fraction of time where outputs of the estimator can safely be used [2, 3]. It is of primary importance for system availability to derive a *tight bound* on the integrity risk.

Therefore, in this research, the objective of the new RAIM method is to reduce the actual integrity risk in the presence of multiple simultaneous faults while providing a tight bound on the integrity risk. To achieve this goal, both the detector and the estimator design are investigated.

In the first part of this paper, the RAIM detector is selected by analyzing RAIM algorithms that have been developed over the past 25 years [4, 5, 6]. Whereas equivalence between parity-based and residual based (RB) methods has been proven [7], most other approaches have only been roughly compared. In this work, two of the most widely implemented RAIM algorithms, RB RAIM and solution separation (SS), are rigorously compared to select the method that minimizes the integrity risk in the presence of single satellite faults and of multiple simultaneous faults.

Two major issues must be addressed when comparing the two RAIM methods. First, practical implementations of RB and SS RAIM differ significantly: in RB RAIM, the integrity risk can directly be evaluated using a single detection test statistic [6], whereas in SS RAIM, protection levels are derived using as many test statistics as fault hypotheses [8, 9]. In order to establish fair grounds for comparison, in this work, the integrity risk contributions using RB and SS RAIM are directly evaluated under each fault hypothesis. Direct integrity risk evaluation also provides tighter integrity risk bounds because the conservative assumptions needed for protection level derivation are avoided. Second, comparisons in the presence of multiple simultaneous faults require that the worst-case fault vector, which maximizes the integrity risk bound, be determined. In this paper, analytical expressions of the worst-case fault vector are derived both for RB and for SS RAIM.

The second part of this research focuses on the estimator design. Over the past decade, researchers have explored the potential of using non-least-squares estimators to reduce the integrity risk at the cost of lower accuracy performance [10, 11, 12]. This concept aims at improving the combined availability of accuracy and integrity, and is motivated by the fact that integrity requirements are often more demanding than accuracy requirements. In this work, the new non-least-squares estimator is numerically determined by solving an integrity risk minimization

problem assuming the presence of multiple simultaneous faults.

Section II of this paper outlines a procedure to handle multiple fault hypotheses for integrity risk evaluation using multi-constellation GNSS. Section III describes the measurement equation, the least-squares estimator and the RB and SS test statistics. A third intermediary algorithm, named full-state solution separation (FS), is developed to facilitate comparisons between RAIM methods. In Section IV, analytical expressions of the worst-case fault vector are derived for RB, FS and SS RAIM. All three RAIM methods are then compared in Section V, which enables the selection of a detector. Section VI presents a numerical method to determine a non-least squares estimator that minimizes the integrity risk. The resulting RAIM algorithm performance is analyzed and evaluated in Section VII in comparison with a SS RAIM method that uses a least-squares estimator.

II. INTEGRITY RISK EVALUATION FOR MULTI-CONSTELLATION GNSS

The integrity risk or probability of hazardous misleading information (HMI) can be expressed considering a set of complementary, mutually exclusive hypotheses. Let n be the number of space vehicles (SV) in view. Each satellite's ranging signal can either be fault-free or in a faulted state. Let i be the index corresponding to fault hypotheses. The total number of hypotheses H_i , including all combinations of fault-free measurements and of multiple simultaneous satellite faults, is 2^n . Using the law of total probabilities, the criterion for availability of integrity can be expressed as:

$$P(HMI) = \sum_{i=0}^{2^n-1} P(HMI | H_i) P(H_i) < I_{REQ} \quad (1)$$

where is I_{REQ} the integrity risk requirement.

Fortunately, only few of the 2^n terms in equation 1 have a substantial impact on $P(HMI)$. To illustrate this statement, the hypotheses H_i can be grouped considering fault-free conditions, single-SV faults, two simultaneous SV faults, and three or more simultaneous faults. The probability of HMI can then be rewritten as:

$$P(HMI) = P(HMI | 0F)P_{0F} + P(HMI | 1F)P_{1F} + P(HMI | 2F)P_{2F} + P(HMI | \geq 3F)P_{\geq 3F} \quad (2)$$

The prior probabilities of single SV fault P_{1F} , of dual SV faults P_{2F} and of three or more simultaneous faults $P_{\geq 3F}$

follow a binomial probability distribution. Indeed, for P_{1F} , the event of single satellite faults regroups n fault hypotheses: fault on the first satellite (named SV1), fault on the second satellite (SV2), ..., fault on the n^{th} satellite (SV n). It can be expressed as:

$$P_{1F} = C_1^n P_{sat} (1 - P_{sat})^{n-1} \quad (3)$$

where C_1^n is the binomial coefficient, and P_{sat} is the prior probability of individual satellite fault, which is assumed independent from one SV to another. In a similar manner, the probabilities P_{2F} and $P_{\geq 3F}$ are given by:

$$P_{2F} = C_2^n P_{sat}^2 (1 - P_{sat})^{n-2} \quad (4)$$

$$P_{\geq 3F} = \sum_{k=3}^n C_k^n P_{sat}^k (1 - P_{sat})^{n-k} \quad (5)$$

In this work, an example value for P_{sat} of 10^{-4} is assumed. It is derived from a satellite failure rate of 10^{-4} /hour specified in [13] and from a time to alert by the GPS Operational Control Segment (OCS) of one hour (the OCS time to alert is guaranteed to be lower than six hours [14], but it is usually much lower; one hour is assumed to be a reasonable value).

The probabilities P_{1F} , P_{2F} , and $P_{\geq 3F}$ are plotted in Fig. 1 versus increasing values of the number of visible satellites. When the number of visible satellites is larger than 6, the prior probabilities P_{1F} and P_{2F} are both above the example integrity risk requirement I_{REQ} of 10^{-7} . This example illustrates that, for multi-constellation GNSS, it is crucial to detect cases of single SV faults as well as cases of two simultaneous faults.

In contrast, $P_{\geq 3F}$ remains orders of magnitude below the requirement. Therefore a bounding assumption on $P(HMI | \geq 3F)$ in equation 2 can be made. The probability $P(HMI | \geq 3F)$ is lower than or equal to 1, so it can be bounded by 1. Finally, the availability criterion in equation 1 can be rewritten, by keeping on the left hand side the probabilities of HMI given fault free conditions and given cases of single and dual SV faults, as:

$$\sum_{i=0}^{n+C_2^n} P(HMI | H_i) P(H_i) < I_{REQ} - P_{\geq 3F} \quad (6)$$

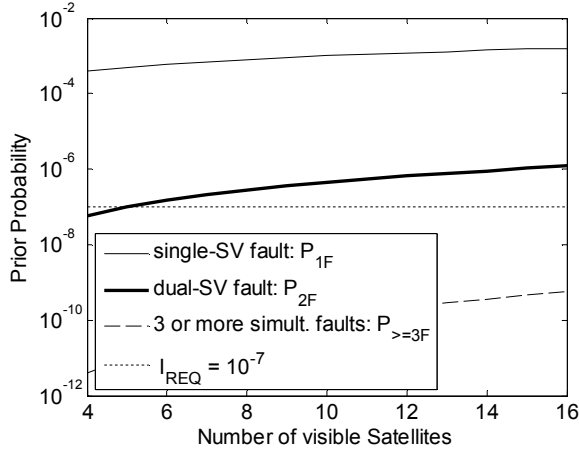


Fig. 1 Prior Probability of Simultaneous Satellite Faults (Assuming $P_{sat} = 10^{-4}$)

Finally, individual terms of the sum in equation 6 can be defined. Let ε be the estimate error for a state of interest (e.g., in aircraft precision approach applications, the vertical position coordinate is of primary concern). Also, let q be the detection test statistic. Given a hypothesis H_i , the probability of HMI is the joint probability of ε being larger than a specified alert limit ℓ while q remains lower than a detection threshold T , which is set to limit the probability of false alarms:

$$P(HMI | H_i) = P(\varepsilon > \ell, |q| < T | H_i) \quad (7)$$

The estimate error ε and the test statistic q are derived in Section III.

III. RAIM USING THE LEAST-SQUARES ESTIMATOR

This section introduces notations describing the least-squares (LS) estimator and RAIM detector, which are used to evaluate the integrity risk defined in equation 7. For comparisons in Section V, three different detection test statistics are investigated: the residual-based (RB) test statistic, the full-state solution-separation (FS) and the single-state solution separation (SS).

A. Measurement Equation

The estimate error ε and test statistic q in equation 7 are evaluated using a measurement model. Let n and m respectively be the numbers of measurements and of states. The $n \times 1$ measurement vector \mathbf{z} is modeled as:

$$\mathbf{z} = \mathbf{H}\mathbf{x} + \mathbf{v} + \mathbf{f} \quad (8)$$

where

- \mathbf{H} is the $n \times m$ observation matrix,
- \mathbf{x} is the $m \times 1$ state vector,
- \mathbf{v} is the $n \times 1$ measurement noise vector, and
- \mathbf{f} is the $n \times 1$ fault vector.

Vector \mathbf{v} is assumed normally distributed, with zero-mean and covariance matrix \mathbf{V} . The following notation is used:

$$\mathbf{v} \sim N(\mathbf{0}, \mathbf{V}). \quad (9)$$

where $\mathbf{0}$ is a matrix of zeros of appropriate dimension (it is an $n \times 1$ vector in this case). Matrix \mathbf{V} is assumed to be diagonal in the proofs of Sections IV and V.

The probability distribution of nominal measurement errors \mathbf{v} can be reliably modeled using large amounts of experimental data. More precisely, this work assumes that the folded cumulative distribution functions of nominal measurement errors are bounded by the Gaussian functions described in equation 9 [15]. In contrast, rare-event sensor faults are difficult to observe because of their low probability of occurrence. In order to avoid making assumptions on unknown fault distributions, a bound on the integrity risk corresponding to the worst case fault vector $\bar{\mathbf{f}}$ can be evaluated. Thus, the fault vector \mathbf{f} can be interpreted as a deterministic measurement bias. And, although the actual fault is unknown, the worst case fault vector $\bar{\mathbf{f}}$, which maximizes the integrity risk bound, is analytically derived in Section IV.

B. Partitioning the Measurement Equation

The assumed number of faulty measurements n_A satisfies the following equation:

$$0 < n_A \leq n - m \quad (10)$$

Equation 10 exposes a fundamental limitation of RAIM, which is only effective when the number of redundant measurements ($n - m$) is larger than n_A . Using ranging signals from multi-constellation GNSS such as GPS/GLONASS or GPS/Galileo ensures that equation 10 is satisfied. First, according to the discussion in Section II, n_A can take values of 1 or 2. Second, the number of redundant measurements ($n - m$) is larger than 2: the number of states m includes three position coordinates and two constellation-dependent receiver clock offsets, while the number of measurements n exceeds eight (four or more per constellation).

The RB, FS, and SS test statistics are derived below for an example hypothesis H_A . Without loss of generality, it

is assumed that faults are simultaneously affecting the first n_A measurements of the measurement vector \mathbf{z} . In anticipation of the solution-separation description, the measurement equation 8 can be partitioned to distinguish the subset of faulty measurements (identified by subscript A) from the fault-free measurements (subscript B):

$$\begin{bmatrix} \mathbf{z}_A \\ \mathbf{z}_B \end{bmatrix} = \begin{bmatrix} \mathbf{H}_A \\ \mathbf{H}_B \end{bmatrix} \mathbf{x} + \begin{bmatrix} \mathbf{v}_A \\ \mathbf{v}_B \end{bmatrix} + \begin{bmatrix} \mathbf{f}_A \\ \mathbf{0} \end{bmatrix} \quad (11)$$

As mentioned above, the covariance matrix \mathbf{V} is assumed diagonal, and can be written as:

$$\mathbf{V} = \begin{bmatrix} \mathbf{V}_A & \mathbf{0} \\ \mathbf{0} & \mathbf{V}_B \end{bmatrix} \quad (12)$$

C. Least-Squares Estimation

The weighted least squares state estimate vector $\hat{\mathbf{x}}$ and its covariance matrix \mathbf{P} (assuming that $n > m$) are given by:

$$\hat{\mathbf{x}} = \mathbf{S}\mathbf{z} \quad \text{and} \quad \mathbf{P} = (\mathbf{H}^T \mathbf{V}^{-1} \mathbf{H})^{-1} \quad (13)$$

where $\mathbf{S} = \mathbf{P}\mathbf{H}^T \mathbf{V}^{-1}$ (14)

The state estimate error vector is defined as:

$$\boldsymbol{\varepsilon} \equiv \hat{\mathbf{x}} - \mathbf{x} = \mathbf{S}(\mathbf{v} + \mathbf{f}) \quad \text{and} \quad \boldsymbol{\varepsilon} \sim \mathcal{N}(\mathbf{S}\mathbf{f}, \mathbf{P}) \quad (15)$$

In parallel, for solution separation, the fault-free subset solution $\hat{\mathbf{x}}_B$ and its covariance matrix \mathbf{P}_B (assuming that $n - n_A \geq m$) are given by:

$$\hat{\mathbf{x}}_B = \mathbf{S}_B \mathbf{z}_B \quad , \quad \mathbf{P}_B = (\mathbf{H}_B^T \mathbf{V}_B^{-1} \mathbf{H}_B)^{-1} \quad (16)$$

where $\mathbf{S}_B = \mathbf{P}_B \mathbf{H}_B^T \mathbf{V}_B^{-1}$ (17)

The fault-free estimate error vector is defined as:

$$\boldsymbol{\varepsilon}_B \equiv \hat{\mathbf{x}}_B - \mathbf{x} = \mathbf{S}_B \mathbf{v}_B \quad \text{and} \quad \boldsymbol{\varepsilon}_B \sim \mathcal{N}(\mathbf{0}, \mathbf{P}_B) \quad (18)$$

Finally, if the focus of the integrity analysis is on a single state of interest (e.g., on the vertical position coordinate for aircraft precision approach navigation), then a single row of the least-squares estimation matrix \mathbf{S} is needed, and is noted:

$$\mathbf{s}^T = \boldsymbol{\alpha}^T \mathbf{S} \quad \text{where} \quad \boldsymbol{\alpha}^T = [\mathbf{0} \quad 1 \quad \mathbf{0}] \quad (19)$$

The following notations will be used:

$$\sigma^2 = \boldsymbol{\alpha}^T \mathbf{P} \boldsymbol{\alpha} \quad \text{and} \quad \sigma_B^2 = \boldsymbol{\alpha}^T \mathbf{P}_B \boldsymbol{\alpha}$$

The scalar estimate error ε that appears in the integrity risk equation 7 under hypothesis H_A can be expressed as:

$$\varepsilon = \boldsymbol{\alpha}^T \boldsymbol{\varepsilon} = \mathbf{s}^T (\mathbf{v} + \mathbf{f}) \quad (20)$$

D. Residual-Based RAIM

The residual vector is defined as:

$$\mathbf{r} \equiv (\mathbf{I} - \mathbf{H}\mathbf{S})\mathbf{z} = (\mathbf{I} - \mathbf{H}\mathbf{S})(\mathbf{v} + \mathbf{f}) \quad (21)$$

where \mathbf{I} is the identity matrix of appropriate dimensions. The residual-based test statistic q_{RB} is the norm of \mathbf{r} weighted by \mathbf{V}^{-1} :

$$q_{RB} = \mathbf{r}^T \mathbf{V}^{-1} \mathbf{r} \quad (22)$$

The scalar random variable q_{RB} follows a non-central chi-square distribution with $(n - m)$ degrees of freedom and non-centrality parameter λ_{RB}^2 . The following notation is used:

$$q_{RB} \sim \chi^2(n - m, \lambda_{RB}^2) \quad (23)$$

with $\lambda_{RB}^2 = \mathbf{f}^T \mathbf{V}^{-1} (\mathbf{I} - \mathbf{H}\mathbf{S}) \mathbf{f}$ (24)

E. Full-State Solution Separation

The full-state solution separation vector is defined as:

$$\boldsymbol{\Delta} \equiv \hat{\mathbf{x}} - \hat{\mathbf{x}}_B \quad (25)$$

$$\boldsymbol{\Delta} = \boldsymbol{\varepsilon} - \boldsymbol{\varepsilon}_B = \mathbf{S}_\Delta \mathbf{z} \quad \text{and} \quad \boldsymbol{\Delta} \sim \mathcal{N}(\mathbf{S}_\Delta \mathbf{f}, \mathbf{P}_\Delta) \quad (26)$$

where $\mathbf{S}_\Delta = \mathbf{S} - \begin{bmatrix} \mathbf{0}_{[m \times n_A]} & \mathbf{S}_B \end{bmatrix}$ (27)

The matrix $\mathbf{0}_{[m \times n_A]}$ is a $m \times n_A$ matrix of zeros. In Appendix I, it is shown that:

$$\mathbf{P}_\Delta = \mathbf{P}_B - \mathbf{P} \quad (28)$$

The full-state solution separation exploits the entire vector $\boldsymbol{\Delta}$ instead of a single state. Single-state solution separation is described in Section III-F. In order to obtain a scalar FS test statistic that can be evaluated and compared with q_{RB} , a weighted norm of $\boldsymbol{\Delta}$ is derived.

The weighting matrix for the norm of $\mathbf{\Lambda}$ is defined as the Moore-Penrose pseudo-inverse \mathbf{P}_Δ^+ of the real, symmetric, rank-deficient matrix \mathbf{P}_Δ (of rank n_A). It is uniquely defined by the following four conditions [16]:

$$\begin{aligned} \mathbf{P}_\Delta \mathbf{P}_\Delta^+ \mathbf{P}_\Delta &= \mathbf{P}_\Delta, \quad \mathbf{P}_\Delta^+ \mathbf{P}_\Delta \mathbf{P}_\Delta^+ = \mathbf{P}_\Delta^+ \\ (\mathbf{P}_\Delta \mathbf{P}_\Delta^+)^T &= \mathbf{P}_\Delta \mathbf{P}_\Delta^+ \quad \text{and} \quad (\mathbf{P}_\Delta^+ \mathbf{P}_\Delta)^T = \mathbf{P}_\Delta^+ \mathbf{P}_\Delta \end{aligned} \quad (29)$$

\mathbf{P}_Δ^+ can be derived numerically using a singular value decomposition of \mathbf{P}_Δ :

$$\mathbf{P}_\Delta = \mathbf{U}_L \mathbf{\Lambda} \mathbf{U}_R \quad (30)$$

Matrix $\mathbf{\Lambda}$ is a diagonal matrix, with diagonal elements the singular values of \mathbf{P}_Δ . Let $\mathbf{\Lambda}^+$ be a diagonal matrix, whose diagonal elements are the inverse of the non-zero diagonal elements of $\mathbf{\Lambda}$, and are zeros otherwise. \mathbf{P}_Δ^+ can be computed as [17]:

$$\mathbf{P}_\Delta^+ = \mathbf{U}_L \mathbf{\Lambda}^+ \mathbf{U}_R \quad (31)$$

Finally, the FS test statistic is defined as:

$$q_{FS} \equiv \mathbf{\Lambda}^T \mathbf{P}_\Delta^+ \mathbf{\Lambda} \quad (32)$$

$$q_{FS} \sim \chi^2(n_A, \lambda_{FS}^2) \quad (33)$$

where
$$\lambda_{FS}^2 = \mathbf{f}^T \mathbf{S}_\Delta^T \mathbf{P}_\Delta^+ \mathbf{S}_\Delta \mathbf{f} \quad (34)$$

F. Single-State Solution Separation

The single-state solution separation extracts a single state out of the solution separation vector:

$$\Delta_{SS} \equiv \mathbf{\alpha}^T \mathbf{\Lambda} \quad (35)$$

$$\Delta_{SS} = \mathbf{s}_\Delta^T \mathbf{z} \quad \text{and} \quad \Delta_{SS} \sim \mathcal{N}(\mathbf{s}_\Delta^T \mathbf{f}, \sigma_\Delta^2) \quad (36)$$

where
$$\mathbf{s}_\Delta^T = \mathbf{\alpha}^T \mathbf{S}_\Delta \quad \text{and} \quad \sigma_\Delta^2 = \mathbf{\alpha}^T \mathbf{P}_\Delta \mathbf{\alpha} = \sigma_B^2 - \sigma^2 \quad (37)$$

Conventional SS algorithms directly compare Δ_{SS} to a detection threshold. Instead, in Sections IV and V, an *equivalent* test statistic is employed, which yields the exact same performance in terms of integrity risk, but which also enables comparisons with q_{RB} and q_{FS} . It is defined as:

$$q_{SS} \equiv \Delta_{SS}^2 / \sigma_\Delta^2 \quad (38)$$

$$q_{SS} \sim \chi^2(1, \lambda_{SS}^2) \quad (39)$$

where
$$\lambda_{SS}^2 = \mathbf{f}^T \mathbf{s}_\Delta \mathbf{s}_\Delta^T \mathbf{f} / \sigma_\Delta^2 \quad (40)$$

G. Summary for the Description of the Least-Squares Estimator and Detectors

Under the multi-measurement fault hypothesis H_A expressed in equation 11, all the elements of the integrity risk equation 7 have been defined. The estimate error ε is given in equation 20 and the three test statistics q_{RB} , q_{FS} and q_{SS} are all expressed as non-centrally chi-square distributed random variables in equations 23, 33 and 39, respectively.

IV. RAIM AGAINST MULTIPLE MEASUREMENT FAULTS

In order to compare RB RAIM with FS and SS in the presence of multiple simultaneous faults, the worst-case fault vector $\bar{\mathbf{f}}$ must be determined for each of the three methods. The term ‘worst-case’ indicates that the fault vector $\bar{\mathbf{f}}$ that maximizes the integrity risk bound.

In general, a fault vector \mathbf{f} can be characterized by:

- the fault hypothesis or fault mode, which identifies the subset of satellites affected by the fault,
- the fault magnitude, which is the Euclidean norm of the fault vector,
- and the fault direction, which is determined by the relative values of the fault vector’s elements.

Fig. 2 presents example fault vectors. The first group of vectors are single-SV fault vectors, modeling fault modes on the first, second and n^{th} satellites (SV1, SV2 and SV n). For single SV faults, it can be noted that the fault direction is fully defined by the fault mode and fault magnitude. This is not the case for multiple simultaneous satellite faults. For example, the last two example vectors are both dual-SV faults simultaneously affecting SV1 and SV2. Their modes and magnitudes are the same, but their direction is different.

Therefore, in the presence of multiple simultaneous faults which are likely to occur in multi-constellation GNSS, it is not only crucial to determine the worst case fault magnitude (as for single SV faults), but also the worst-case direction, which maximizes the integrity risk.

$$\underbrace{\begin{bmatrix} 1 \\ 0 \\ 0 \\ \vdots \\ 0 \end{bmatrix}, \begin{bmatrix} 0 \\ 1 \\ 0 \\ \vdots \\ 0 \end{bmatrix}, \dots, \begin{bmatrix} 0 \\ 0 \\ \vdots \\ 1 \end{bmatrix}}_{\text{single SV faults}}, \underbrace{\begin{bmatrix} 1 \\ 2 \\ 0 \\ \vdots \\ 0 \end{bmatrix}, \begin{bmatrix} 2 \\ 1 \\ 0 \\ \vdots \\ 0 \end{bmatrix}, \dots}_{\text{dual SV faults}}$$

Fig. 2 Example Fault Vectors

As expressed in equations 15, 24, 34 and 40, the fault vector \mathbf{f} impacts the mean of ε and the non-centrality parameters of q_{RB} , q_{FS} and q_{SS} . It has been shown in [18, 19] that the worst case fault vector $\bar{\mathbf{f}}$ maximizes the square of the failure mode slope g_F^2 , which is independent of the fault magnitude, and is defined as the ratio of the squared mean of the estimate error over the non-centrality parameter of the test statistic:

$$g_F^2 \equiv \frac{\mathbf{f}^T \mathbf{s} \mathbf{s}^T \mathbf{f}}{\mathbf{f}^T \mathbf{M}_{DENOM} \mathbf{f}} \quad (41)$$

where

$$\begin{aligned} \mathbf{M}_{DENOM} &= \mathbf{V}^{-1}(\mathbf{I} - \mathbf{H}\mathbf{S}) && \text{for RB RAIM} \\ \mathbf{M}_{DENOM} &= \mathbf{S}_\Delta^T \mathbf{P}_\Delta^+ \mathbf{S}_\Delta && \text{for FS} \\ \mathbf{M}_{DENOM} &= \mathbf{s}_\Delta \mathbf{s}_\Delta^T / \sigma_\Delta^2 && \text{for SS} \end{aligned}$$

The following notation is used to express the non-zero elements of fault vector \mathbf{f} under hypothesis H_A (H_A is described in equation 11):

$$\mathbf{f} = \mathbf{A} \mathbf{f}_A \quad \text{with} \quad \mathbf{A} \equiv \begin{bmatrix} \mathbf{I}_{n_A} \\ \mathbf{0} \end{bmatrix} \quad (42)$$

where \mathbf{I}_{n_A} is a $n_A \times n_A$ identity matrix. It is worth noticing for upcoming derivations, that

$$\mathbf{S}_\Delta \mathbf{A} = \mathbf{S} \mathbf{A} \quad (43)$$

which is obvious from the definitions of \mathbf{S}_Δ and \mathbf{A} in equations 27 and 42, respectively.

Equation 41 can be rewritten using the definition of \mathbf{A} and using a change of variables [18, 19]:

$$\mathbf{f}_A = \mathbf{M}_A \mathbf{f}_{A^*} \quad (44)$$

$$g_F^2 = \frac{\mathbf{f}_{A^*}^T \mathbf{M}_A^T \mathbf{M}_X^T \mathbf{M}_X \mathbf{M}_A \mathbf{f}_{A^*}}{\mathbf{f}_{A^*}^T \mathbf{f}_{A^*}} \quad (45)$$

where

$$\begin{aligned} \mathbf{M}_X &= \mathbf{s}^T \mathbf{A} \\ \mathbf{M}_A &= (\mathbf{A}^T \mathbf{V}^{-1} (\mathbf{I} - \mathbf{H}\mathbf{S}) \mathbf{A})^{-1/2} && \text{for RB RAIM} \\ \mathbf{M}_A &= (\mathbf{A}^T \mathbf{S}^T \mathbf{P}_\Delta^+ \mathbf{S} \mathbf{A})^{-1/2} && \text{for FS} \\ \mathbf{M}_A &= \left((\mathbf{A}^T \mathbf{s} \mathbf{s}^T \mathbf{A} / \sigma_\Delta^2)^+ \right)^{1/2} && \text{for SS} \end{aligned}$$

It follows that the worst-case fault vector $\bar{\mathbf{f}}$ can be expressed as [18, 19]:

$$\bar{\mathbf{f}} = \mathbf{A} \mathbf{M}_A \mathbf{v}_{MAX} \quad (46)$$

where \mathbf{v}_{MAX} is the eigenvector corresponding to the maximum eigenvalue of:

$$\mathbf{M}_A^T \mathbf{M}_X^T \mathbf{M}_X \mathbf{M}_A \quad (47)$$

For comparisons between the three RAIM methods in Section V, the expression of $\bar{\mathbf{f}}$ in terms of \mathbf{v}_{MAX} , which is numerically determined, is insufficient. In response, an analytical expression of \mathbf{v}_{MAX} is derived. Let matrix \mathbf{M} be defined as:

$$\mathbf{M} = \mathbf{M}_A^T \mathbf{M}_X^T (\mathbf{M}_X \mathbf{M}_A \mathbf{M}_A^T \mathbf{M}_X^T)^{-1} \mathbf{M}_X \mathbf{M}_A \quad (48)$$

Matrix \mathbf{M} is the expression of equation 47 multiplied by the ‘normalizing factor’ $(\mathbf{M}_X \mathbf{M}_A \mathbf{M}_A^T \mathbf{M}_X^T)^{-1}$. It can easily be shown that \mathbf{M} is symmetric and idempotent:

$$\mathbf{M} = \mathbf{M}^T \quad \text{and} \quad \mathbf{M} = \mathbf{M} \mathbf{M} \quad (49)$$

Matrix \mathbf{M} is called an orthogonal projector and is derived from an inner product $(\mathbf{M}_A^T \mathbf{M}_X^T$ in equation 48 is a $n_A \times 1$ vector). Therefore, \mathbf{M} has a single non-zero eigenvalue, of value 1. It follows that the matrix in equation 47 has a single non-zero eigenvalue, of value the inverse of the normalizing factor used in equation 48. This provides an expression of the worst-case failure mode slope \bar{g}_F^2 :

$$\bar{g}_F^2 = \mathbf{M}_X^T \mathbf{M}_A \mathbf{M}_A^T \mathbf{M}_X^T \quad (50)$$

In addition, the worst-case fault vector direction coincides with the direction of the line that \mathbf{M} is projecting onto. This direction is given by $\mathbf{M}_A^T \mathbf{M}_X^T$. The conclusion of

this section is that the worst-case fault direction $\bar{\mathbf{f}}$ under a multi-measurement fault hypothesis H_A is given by:

$$\bar{\mathbf{f}} = \mathbf{A}\mathbf{M}_A\mathbf{M}_A^T\mathbf{M}_X^T \quad (51)$$

Section V will further show that the worst-case failure mode slope \bar{g}_F^2 is the same for SS, FS and RB RAIM, and that its value is the variance of the solution separation σ_Δ^2 . Equations 50 and 51 are essential not only for the comparison in Section V, but also for direct integrity risk evaluation in the presence of multiple simultaneous faults in Section VI.

V. SOLUTION SEPARATION VERSUS RESIDUAL-BASED RAIM USING THE LEAST-SQUARES ESTIMATOR

The comparison between RB, FS, and SS RAIM is performed in two steps. In Section V-A, the integrity risk is evaluated for a theoretical case assuming that there is only one fault hypothesis, i.e., a single term in the sum in equation 6. For notation purposes and without loss of generality, the single hypothesis is the multi-measurement fault hypothesis H_A defined in equation 11. The analysis is then extended to include all fault hypotheses in Section V-B.

A. Single Hypothesis Assumption

Under hypothesis H_A , direct analytical comparisons of q_{RB} , q_{FS} and q_{SS} show, in Appendices II and III, that the three methods are equivalent if and only if:

$$n_A = n - m = 1 \quad (52)$$

Establishing these results requires that an identity be derived for the pseudo-inversion of a rank-deficient matrix (proof in Appendix IV):

$$\mathbf{H}_A\mathbf{P}\mathbf{P}_\Delta^+\mathbf{P}\mathbf{H}_A^T = \mathbf{H}_A\mathbf{P}\left(-\mathbf{P}^{-1} - \mathbf{P}^{-1}(\mathbf{P}_B^{-1} - \mathbf{P}^{-1})^+\mathbf{P}^{-1}\right)\mathbf{P}\mathbf{H}_A^T$$

Therefore, in general, RB, FS, and SS RAIM are not equivalent. The remainder of this section aims at selecting the test statistic that generates the smallest integrity risk.

In this perspective, Appendix V shows that the least-squares (LS) estimate error ε is independent from the test statistic q for all three methods, so that the joint probability in equation 7 can be written as a product of probabilities:

$$P(HMI | H_A) = P(|\varepsilon| > \ell | H_A)P(q < T | H_A) \quad (53)$$

where q is a placeholder for either q_{RB} , q_{FS} or q_{SS} . The Appendix V-C shows that, for LS estimators, the proof of independence with ε can be extended to *any* test statistic q that maps measurements into the null space of the observation matrix transposed \mathbf{H}^T (also called parity space).

The probability of no detection $P(q < T | H_A)$ in equation 53 is evaluated considering the test statistics' distributions in equations 23, 33 and 39:

$$\begin{aligned} q_{RB} &\sim \chi^2(n-m, \lambda_{RB}^2) \\ q_{FS} &\sim \chi^2(n_A, \lambda_{FS}^2) \\ q_{SS} &\sim \chi^2(1, \lambda_{SS}^2) \end{aligned}$$

Appendix VI-A shows that the bounds on the non-centrality parameters corresponding to $\bar{\mathbf{f}}$ (derived in Section IV) are equivalent for RB and FS:

$$\bar{\lambda}_{RB}^2 = \bar{\lambda}_{FS}^2 \quad (54)$$

Appendix VI-B also proves that the worst-case fault slope \bar{g}_F is the same for all three RAIM methods, and that:

$$\bar{g}_F^2 = \sigma_\Delta^2 \quad (55)$$

A generalization is performed in Appendix VI-C to find the test statistic (mapping measurements in the parity space) that minimizes the worst-case slope \bar{g}_F . It is proved for single-SV faults, that RB, FS and SS all minimize the worst-case fault slope σ_Δ^2 , and that their test statistics are derived from vectors aligned with the 'characteristic fault mode lines' in the parity space [20, 21].

Equation 55 states that the relative impact on ε and q of the worst-case fault vector $\bar{\mathbf{f}}$ is the same for all three methods. Thus, since the same estimator is implemented in all three RAIM methods, the probability of hazardous information $P(|\varepsilon| > \ell | H_A)$ in equation 53 does not influence the comparison. The analysis hence narrows down to evaluating $P(q < T | H_A)$ for the three test statistics.

It follows from equations 23, 33, 39, and 55 that q_{RB} , q_{FS} and q_{SS} all follow non-central chi-square distributions,

with the same non-centrality parameter bound $\bar{\lambda}^2$, but with different numbers of degrees of freedom: $n-m$, n_A , and 1, respectively.

This difference has an impact on the spread of the distribution, which is addressed below in Section V-B. But, the most decisive impact is on the detection thresholds (T in equation 53), which vary greatly from one method to the other. Detection thresholds T_{RB} , T_{FS} , and T_{SS} are set in compliance with a continuity risk requirement P_{CONT} to limit the probability of alarms under fault-free conditions (i.e., when $\bar{\lambda}^2=0$), and are respectively defined for RB, FS and SS as:

$$\int_{T_{RB}}^{+\infty} \chi_q^2(n-m, 0) dq = P_{CONT} \quad (56)$$

$$\int_{T_{FS}}^{+\infty} \chi_q^2(n_A, 0) dq = P_{CONT} \quad (57)$$

$$\int_{T_{SS}}^{+\infty} \chi_q^2(1, 0) dq = P_{CONT} \quad (58)$$

Because, in general, the following inequalities are true:

$$n-m \geq n_A \geq 1 \quad (59)$$

then, the following inequalities are also satisfied:

$$T_{RB} \geq T_{FS} \geq T_{SS} \quad (60)$$

The results obtained in this section are summarized and represented in Fig. 3. Fig. 3 is a ‘failure mode plot’, which represents the estimate error ε versus the square root of the test statistic q (that stands for q_{RB} , q_{FS} or q_{SS}). As the fault magnitude varies, the mean of ε and the non-centrality parameter $\bar{\lambda}$ of $q^{1/2}$ describe a line passing through the origin, with slope \bar{g}_F (which is identical for RB, FS and SS, and is equal to σ_Δ). The alert limit ℓ and detection thresholds T define the boundaries of the HMI area in the upper left-hand quadrant (shadowed). In this case, the larger the HMI area is, the higher the integrity risk becomes. Therefore, the best of the three test statistics is q_{SS} whose threshold T_{SS} is the smallest as expressed in equation 60.

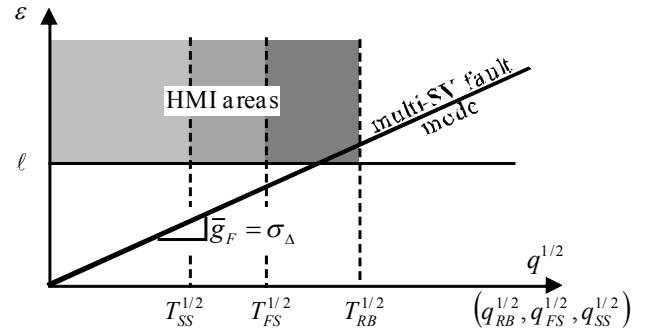


Fig. 3 Failure Mode Plot Summarizing the Findings of the Comparison of RB, FS and SS RAIM (Assuming a Single Hypothesis)

The difference in the numbers of degrees of freedom of q_{RB} , q_{FS} and q_{SS} can be interpreted as follows:

- FS performs better than RB RAIM because FS is tailored to hypothesis H_A
- SS performs better than FB and RB RAIM because SS is not only tailored to hypothesis H_A , but also to the state of interest

All three methods are identically impacted by the worst-case fault vector $\bar{\mathbf{f}}$, but SS exploits knowledge of H_A and of the state of interest to reduce the impact of nominal noise (which is accounted for in the detection thresholds). In addition, considering the results of Appendix VI-C (showing, for single-SV faults, that SS minimizes \bar{g}_F), it is concluded that, under H_A , SS minimizes the integrity risk when a LS estimator is implemented.

However, until this point, only one hypothesis was considered. The full integrity risk equation expressed in equation 6 is a sum of terms corresponding to multiple hypotheses. Also, the difference in the numbers of degrees of freedom also impacts the spread of the distribution (not represented in Fig. 3). These two additional elements are addressed in Section V-B.

B. Considering All Fault Hypotheses

The fact that the integrity risk must be evaluated over multiple hypotheses is expressed in equation 6, which is repeated here:

$$\sum_{i=0}^{n+C_F^2} P(HMI | H_i) P(H_i) < I_{REQ} - P_{\geq 3F}$$

In this section, the comparison focuses on RB versus SS RAIM (the ‘intermediary’ FS method is no longer needed). Let H_0 in equation 6 be the fault-free

hypothesis, and let $n_H = n + C_2^n$ be the number of fault hypotheses. The definition of the RB detection threshold given in equation 56 can be rewritten as:

$$P(q_{RB} \geq T_{RB} | H_0) = P_{CONT} \quad (61)$$

In contrast with RB RAIM where a single test statistic is computed for all fault hypotheses H_i ($i=1, 2, \dots, n_H$), SS requires that a test statistic q_i be computed for each hypothesis H_i . The threshold definition must take into all possible combinations of q_i being greater or lower than the detection threshold T_i .

Therefore, using the law of total probability, the detection thresholds in SS are defined as:

$$P(1FA | H_0) + P(2FA | H_0) + \dots + P(n_H FA | H_0) = P_{CONT} \quad (62)$$

where

- 1FA regroups the events of a single false alarm
- 2FA designates hypotheses of two simultaneous false alarms
- $n_H FA$ occurs when all thresholds are simultaneously exceeded

The expressions of the left-hand-side terms in equation 62 are derived in Appendix VII. For example, the simplest expression is that of the last term:

$$P(n_H FA | H_0) = P(q_1 \geq T_1, q_2 \geq T_2, \dots, q_{n_H} \geq T_{n_H} | H_0)$$

Evaluating equation 62 exactly as a sum of joint probabilities requires that the correlation between test statistics q_i be determined. Instead, for comparison with RB RAIM, two extreme cases are considered:

- fully-correlated q_i : this is the most favorable case for SS when comparing RB versus SS.
- fully-uncorrelated q_i : this is the most unfavorable case for SS versus RB, and the most conservative case for SS.

In the theoretical case of fully-correlated q_i , all test statistics are equivalent, and it is sufficient to consider a single hypothesis. The conclusion under this assumption is the same as in Section V-A: with regard to integrity risk, SS performs better than RB RAIM.

In the conservative case of fully-uncorrelated q_i , the continuity risk requirement P_{CONT} is allocated amongst the n_H test statistics. This allocation must take into

account all the events described in equation 62 (i.e., all combinations of q_i greater or lower than T_i). Appendix VII shows that, assuming equal allocation P_{CONTi} and neglecting the second to n_H^{th} terms in equation 62, the overall allocation can simply be selected as:

$$P_{CONTi} = P_{CONT} / n_H \quad (63)$$

Under these assumptions, the detection thresholds T_i are all equal for $i=1, 2, \dots, n_H$, and are noted T_{SS} . The threshold T_{SS} is defined as:

$$P(q_i \geq T_{SS} | H_0) = P_{CONTi} \quad (64)$$

Values of T_{SS} are plotted in Fig. 4 (thick solid line) as a function of the number of satellites n (along the x-axis), which determines the number of fault hypotheses n_H . The RB threshold T_{RB} is represented for comparison (thin dashed line). It quickly becomes much larger than the T_{SS} (as suggested in Fig. 3 in Section V-A).

The y-axis in Fig. 4 is also used to represent varying values of the non-centrality parameter. This enables to represent the probability of no detection in the presence of faults, i.e., $P(q < T | H_i)$. The shadowed area represents the area where SS performs better than RB RAIM in the sense that:

$$P(q_{RB} < T_{RB} | H_i) > P(q_i < T_{SS} | H_i) \quad (65)$$

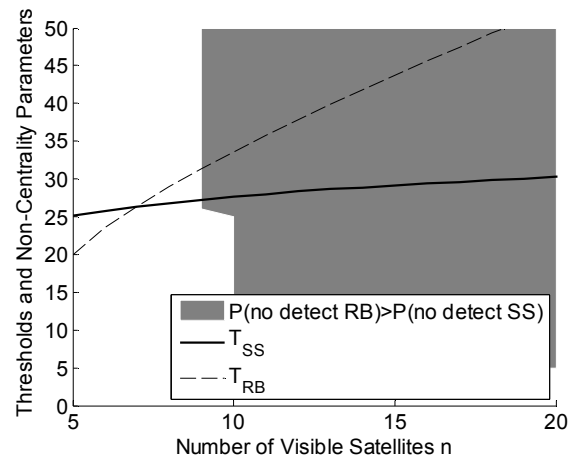


Fig. 4 Comparison of RB with SS RAIM Considering Multiple Fault Hypotheses

Given a hypothesis H_i , the probability of HMI increases as the non-centrality parameter value approaches the threshold value. Fig. 4 shows that, for non-centrality parameter values near the thresholds T_{RB} and T_{SS} , the probability of no detection is higher using RB RAIM than using SS RAIM when the number of visible satellites exceeds nine or ten, which will most often be the case in multi-constellation GNSS.

Therefore, the same conclusion can be drawn, whether the SS test statistics q_i are assumed fully correlated or fully uncorrelated, and this despite conservative assumptions: SS provides better detection capability than RB RAIM.

From a practical point of view, it is worth noticing that RB RAIM may be better adapted under limited computational resources (it is especially the case using sequential RAIM implementations [19]).

C. Intermediary Conclusion: Choice of a Detector

This work aims at deriving an algorithm that minimizes the integrity risk. In this regard, sections V-A and V-B have shown that, when processing measurements from multiple GNSS constellations using a LS estimator, SS performs better than RB RAIM. In addition, the least-squares (LS) SS test statistic can be expressed as a normally distributed random variable, with unit variance:

$$q_s \equiv \Delta / \sigma_\Delta \quad (66)$$

The fact that q_s follows a normal distribution will be exploited in Section VI-A. Equation 66 defines the LS SS test statistic used in the remainder of this paper.

VI. NON-LEAST-SQUARES ESTIMATOR DESIGN TO MINIMIZE THE INTEGRITY RISK

In the first part of this paper, a detector was selected. The second part of this work aims at deriving a modified estimator that minimizes the integrity risk.

A. Non-Least-Squares Estimator Design

As mentioned in Section I, multiple researchers have recently investigated the possibility of using non-LS estimators in RAIM [10, 11, 12]. The objective of these methods is to reduce the integrity risk at the cost of lower accuracy performance in applications where integrity requirements are more stringent than accuracy requirements.

In particular, the non-least squares (NLS) state estimate for the state of interest is expressed in [12] as:

$$\hat{x}_{NLS} \equiv \mathbf{s}^T \mathbf{z} + \boldsymbol{\beta}^T \mathbf{Q} \mathbf{z} \quad (67)$$

where

$\mathbf{s}^T \mathbf{z}$ is the LS estimate for the state of interest

\mathbf{Q} is the $(n-m) \times n$ parity matrix

$\boldsymbol{\beta}$ is the $(n-m) \times 1$ parameter vector that needs to be determined

The state estimate \hat{x}_{NLS} is a sum of two terms. The first term is simply the LS state estimate, i.e., a component of the measurement vector \mathbf{z} laying in the range space of the observation matrix \mathbf{H} . The second term is a component of \mathbf{z} taken in the parity space, and expressed using the parity matrix \mathbf{Q} (e.g., defined in [7]) pre-multiplied by a design parameter vector $\boldsymbol{\beta}^T$, which is determined below to minimize the integrity risk. By definition, \mathbf{Q} satisfies the following equations:

$$\mathbf{Q} \mathbf{H} = \mathbf{0} \quad \text{and} \quad \mathbf{Q} \mathbf{Q}^T = \mathbf{I} \quad (68)$$

The state estimate error is defined as:

$$\varepsilon_{NLS} \equiv \hat{x}_{NLS} - x \quad (69)$$

Substituting the measurement equation 8 into 69 and substituting equation 68 into the resulting expression shows that the estimator in equation 67 is unbiased: ε_{NLS} is not a function of x , which is highly desirable for navigation application. The estimate error can be expressed as:

$$\varepsilon_{NLS} \equiv (\mathbf{s}^T + \boldsymbol{\beta}^T \mathbf{Q}) (\mathbf{v} + \mathbf{f}) \quad (70)$$

This paper builds upon the work by Blanch in [12]. However, Section VI-B directly uses the integrity risk bound instead of protection levels used in [12]. The SS protection level derivation carried out in Appendix VIII singles out the conservative assumption, which is avoided Section VI-B. Therefore, a tighter bound on the integrity risk as compared to [12] is provided below. But, this comes at the expense of a heavier computational load. In addition, graphical representations of the algorithm are introduced, which may be exploited in future work.

The estimator described in equation 67 is not a least squares estimator. Therefore, the new estimate error ε_{NLS} and test statistic q_s are no longer independent (as indicated in Appendix V-C). It follows that the integrity risk can no longer be evaluated as a product of probabilities, and must be treated as a joint probability as expressed in equation 7. Fortunately, numerical methods are now available to compute joint probabilities for

bivariate normally distributed random vectors [22]. This is in part the reason why the test statistic q_S had to be expressed as a normally distributed random variable in equation 66.

The estimate error ε_{NLS} and test statistic q_S can be arranged in a bivariate normally distributed random vector defined as:

$$\boldsymbol{\eta} \equiv \begin{bmatrix} \varepsilon_{NLS} & q_{SS} \end{bmatrix}^T \quad (71)$$

$$\boldsymbol{\eta} \sim N_{\boldsymbol{\eta}}(\boldsymbol{\mu}_{\boldsymbol{\eta}}, \mathbf{P}_{\boldsymbol{\eta}}) \quad (72)$$

where

$$\boldsymbol{\mu}_{\boldsymbol{\eta}} = \begin{bmatrix} \mathbf{s}^T \\ \mathbf{s}_{\Delta^*}^T \end{bmatrix} \mathbf{f} + \begin{bmatrix} \boldsymbol{\beta}^T \mathbf{Q} \\ \mathbf{0} \end{bmatrix} \mathbf{f} \quad (73)$$

$$\mathbf{P}_{\boldsymbol{\eta}} = \begin{bmatrix} \sigma^2 & \mathbf{0} \\ \mathbf{0} & 1 \end{bmatrix} + \begin{bmatrix} \boldsymbol{\beta}^T \mathbf{Q} \mathbf{V} \mathbf{Q}^T \boldsymbol{\beta} & \boldsymbol{\beta}^T \mathbf{Q} \mathbf{V} \mathbf{s}_{\Delta^*} \\ \mathbf{s}_{\Delta^*}^T \mathbf{V} \mathbf{Q}^T \boldsymbol{\beta} & \mathbf{0} \end{bmatrix} \quad (74)$$

with

$$\mathbf{s}_{\Delta^*}^T = \mathbf{s}_{\Delta}^T / \sigma_{\Delta}$$

The mean $\boldsymbol{\mu}_{\boldsymbol{\eta}}$ and covariance $\mathbf{P}_{\boldsymbol{\eta}}$ of $\boldsymbol{\eta}$ were written as sums in order to isolate terms that are a function of the design parameter vector $\boldsymbol{\beta}$.

The impact of $\boldsymbol{\beta}$ is further analyzed using a failure mode plot in Fig.5. A single hypothesis is considered to start the explanation. The HMI area, failure mode line and failure mode slope \bar{g}_F have been defined in Fig.3. The influence of $\boldsymbol{\beta}$ is explained by comparing the new algorithm to SS RAIM using the LS estimator (i.e., using $\boldsymbol{\beta} = \mathbf{0}$). The new method is represented in red, whereas the black color is used for LS estimator-based RAIM. In both cases, lines of constant joint probability density are ellipses because the estimate errors and q_S are normally distributed. The LS estimate error, noted ε_{LS} , and q_S are statistically independent, so that the major axis of the black ellipse is either horizontal, or vertical.

The new method provides the means to move the red ellipse away from the HMI area, hence reducing the integrity risk. The influence of the design parameter vector $\boldsymbol{\beta}$ is threefold:

- The fact that $\boldsymbol{\beta}$ impacts the mean of the estimate error in equation 73 enables to reduce the failure mode slope \bar{g}_{F^*} , which decreases the integrity risk.

- Off diagonal components of the covariance matrix $\mathbf{P}_{\boldsymbol{\eta}}$ are also a function of $\boldsymbol{\beta}$, which enables to modify the red ellipse's orientation, and hence again to reduce the integrity risk.
- However, $\boldsymbol{\beta}$ causes the diagonal element of $\mathbf{P}_{\boldsymbol{\eta}}$ corresponding to the estimate error to increase, which means that the red ellipse is inflated along the minor axis in Fig.5. This negative impact needs to be dealt with.

In addition, the increase in the variance of ε_{NLS} shows that the cost of lowering the integrity risk is a decrease in accuracy performance.

The explanation in Fig. 5 only accounts for a single hypothesis. The parameter vector $\boldsymbol{\beta}$ that minimizes the integrity risk given a hypothesis could cause extremely large increases in integrity risk given other hypotheses. The estimator design parameter vector $\boldsymbol{\beta}$ must therefore be derived to reduce the entire integrity risk equation 6, considering all hypotheses.

Numerical Determination Using a Modified Newton Method

The objective stated above can be formulated in a single minimization problem:

$$\min_{\boldsymbol{\beta}} \sum_{i=0}^{n+C_2^n} \max_{f_i} P\left(|\varepsilon_{NLS}| > \ell, |q_{S,i}| < T_S \mid H_i, f_i\right) P(H_i) \quad (75)$$

The method outlined in this section aims at finding the vector $\boldsymbol{\beta}$ that minimizes the integrity risk. In the same manner as in equation 6, equation 75 expresses the integrity risk as a sum of joint probability distributions, which can be evaluated numerically [22].

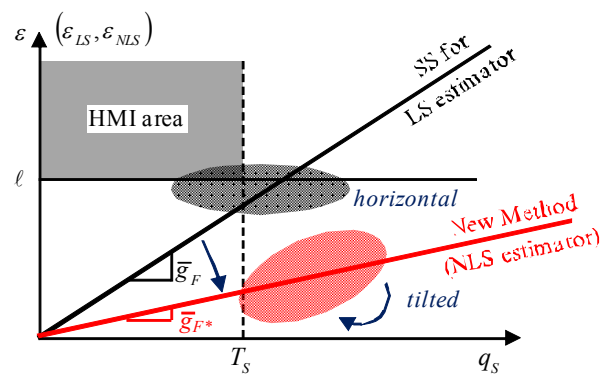


Fig. 5 Failure Mode Plot Illustrating the New Method as Compared to SS RAIM using a LS Estimator

Equation 75 is actually a bound on the integrity risk for the worst-case fault magnitude f_i . The worst case fault direction is also implicitly considered for multi-SV faults. In this regard, the analytical derivation of the worst-case fault direction performed in Section IV becomes instrumental when trying to solve the problem posed in equation 75.

In this paper, we make the conjecture that the minimization problem in equation 75 is convex. This conjecture was numerically verified. In addition, the method used in [12] gives strong indications that the hessian of the objective function in equation 75 can be expressed analytically, and that it can be shown to be positive definite.

This minimization problem can be solved numerically using a modified Newton method [23]. At this stage of this research, the gradient and hessian of the objective function in equation 75 were established numerically [23], which is computationally expensive. But future implementations will address this issue, for example, following a procedure similar to that employed in [12]. In all cases presented in Section VII, convergence of the modified Newton method was achieved in less than 10 iterations.

VII. PERFORMANCE ANALYSIS

This section aims at quantifying the integrity risk reduction obtained using the new NLS estimator as compared to using the LS estimator.

In this preliminary analysis, the two methods are evaluated assuming uncorrelated ranging measurements with 1 m standard deviation ($\mathbf{V} = \mathbf{I}$). Example navigation requirements include a 10^{-7} integrity risk requirement I_{REQ} , a $8 \cdot 10^{-6}$ continuity risk requirement

P_{CONT} , and a 10 m alert limit ℓ . Due to the simple error modeling assumptions, availability performance results presented in Section VII-B are not representative of realistic positioning performance. But Section VII-B illustrates the improvement achieved using the new method as compared to using the LS estimator.

A. Performance Analysis for a Single Satellite Geometry

The new algorithm's underlying mechanisms are first detailed using an illustrative example satellite geometry represented in an azimuth-elevation plot of the sky in Fig. 6. In this example, nine satellites are visible. The next paragraphs focus on two single-satellite fault cases affecting two low elevation satellites (SV7 and SV9). Cases of multiple simultaneous faults are later accounted for in the overall integrity risk evaluation.

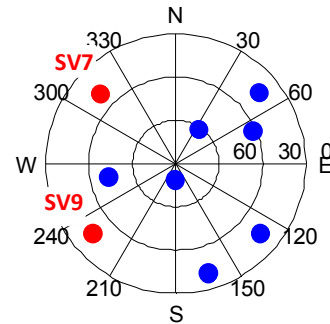


Fig. 6 Azimuth-Elevation Plot For An Example Satellite Geometry

Fig. 7, 8 and 9 present failure mode plots introduced earlier in Fig. 3 and 5. The same color code as in Fig. 5 is employed: failure mode lines and ellipses of constant joint probability density are red for the new method and black using the LS estimator. Ellipses are labeled in terms of $-10 \log P(HMI | H_i)$ to distinguish different levels of probability density. The 10^{-4} joint probability density level is emphasized for illustration purposes.

Fig. 7 shows joint probability distributions for the hypothesis of a single-satellite fault on SV7. This is the fault mode for which the highest fault slope \bar{g}_F was observed using the LS estimator. Because of this large fault slope \bar{g}_F , the black ellipse overlaps the HMI area (for the 10^{-4} joint probability density level). In contrast, using the new method, the red fault mode line has a gentler slope \bar{g}_{F^*} , so that the red ellipse avoids penetrating the HMI area.

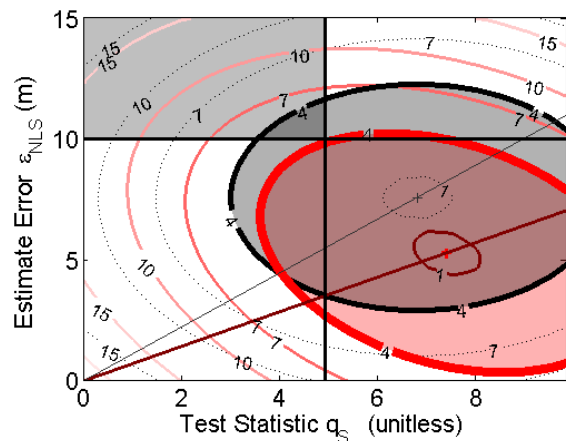


Fig. 7 Example Failure Mode Plot for the Single-SV Fault Hypothesis on SV7 (Worst Slope Using LS)

Fig. 8 presents the case of a single-SV fault on SV9, for which the highest fault slope \bar{g}_{F^*} was observed using the new method in red. The fault slope \bar{g}_{F^*} is actually higher than the original slope \bar{g}_F using the LS estimator. However, the red ellipse's orientation has been modified so that it does not extend over the HMI area.

Fig. 7 and 8 show two mechanisms through which the new algorithm avoids penetrating the HMI area. The new method reduces the integrity risk in Fig. 7, but it does the opposite in Fig. 8. This is because the new method aims at minimizing the integrity risk over all hypotheses. This concept is represented in Fig. 9, where ellipses for all single-SV fault modes are represented. Dual-SV fault modes were included in the computation but not displayed for clarity of exposition. Fig. 9 shows one black ellipse (using the LS estimator) overlapping the HMI area, whereas none of the red ellipses do. This is the ultimate illustration of the new method's performance improvement.

In this example, considering cases of one and two simultaneous faults (totaling 46 hypotheses), the integrity risk decreases from $1.5 \cdot 10^{-7}$ for the LS estimator to $1.2 \cdot 10^{-8}$ using the new method. The price to pay for that integrity risk reduction is an increase in the estimated vertical position coordinate standard deviation from 1.23 m using the LS estimator to 1.30 m using the new method.

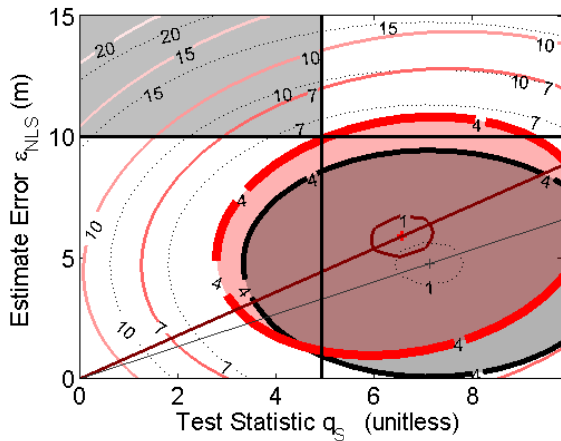


Fig. 8 Failure Mode Plot for the Single-SV Fault Hypothesis on SV9 (Worst Slope Using NLS)

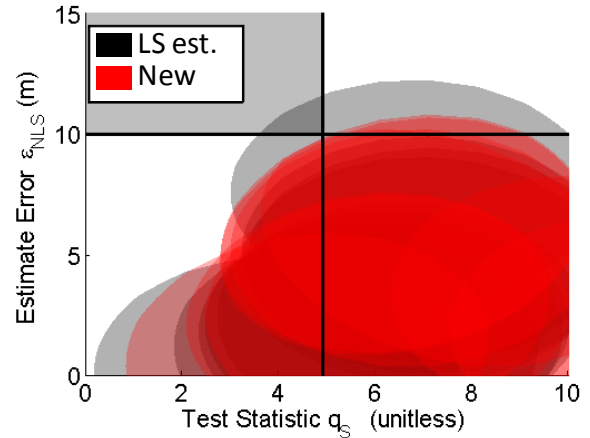


Fig. 9 Failure Mode Plot Displaying all Single-SV Fault Hypotheses

B. Availability Performance Evaluation

In order to illustrate the impact of changes in satellite geometries, the new RAIM method and the one that uses the LS estimator are evaluated at the Miami location, at regular 5 min intervals over a 24 hour period. A nominal 24 GPS satellite constellation and a nominal 27 Galileo satellite constellation are considered [1].

The integrity risk and vertical positioning standard deviation using both methods are plotted in Fig 10. For clarity of exposition, Fig. 10 shows the results at the 17 instances (out of 288 discrete times) where the LS estimator-based method was not meeting the example 10^{-7} integrity risk requirement. In Fig. 10-a, the red curve representing the new method remains mostly below the requirement, whereas the black curve does not.

In parallel, Fig 10-b shows that the vertical position standard deviation is inflated by an average factor of 1.07 using the new method, which may be acceptable in many high-integrity applications. For example, assuming a 4 m accuracy limit, the combined availability of integrity and accuracy (over 24 hrs at Miami) is 99.6% using the new method versus 94.1% using a LS estimator. Fig. 10 illustrates potential performance improvements that can be achieved using non-LS estimators in multi-constellation RAIM (in the presence of multiple simultaneous faults).

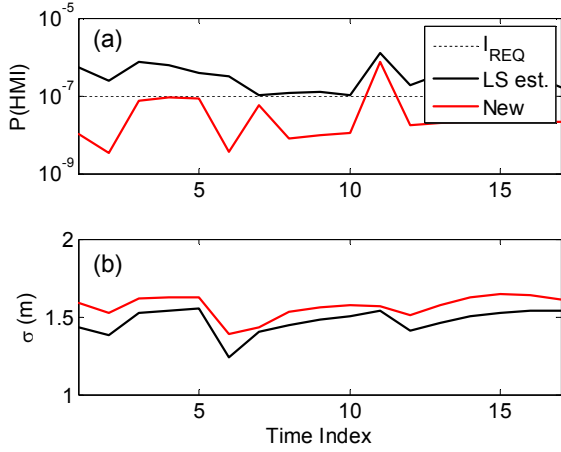


Fig. 10 Evaluation of (a) the Integrity Risk and (b) the Vertical Positioning Standard Deviation Using the New Method (Red) Vs. the LS Estimator (Black)

VIII. CONCLUSION

This paper describes the development of a RAIM method whose detector and estimator are designed to minimize the integrity risk for navigation applications based on future multi-constellation GNSS.

In the first part of this paper, analytical expressions are derived of the worst-case fault direction, which maximizes the integrity risk bound in the presence of multiple simultaneous faults. These analytical results enable to address two major challenges. First, they provide the means to rigorously compare solution separation (SS) and residual-based (RB) RAIM. The paper shows that unlike for RB RAIM, the SS test statistic is tailored to the hypothesis and to the state of interest. Therefore SS reduces the integrity risk as compared to RB RAIM. In addition, analytical expressions of the worst-case faults enable to solve the integrity risk minimization problem, which is formulated in this work to design a new estimator.

Then, the new RAIM method is devised, using the least-squares (LS) SS test statistic for the detector, and using a numerically-determined non-LS estimator that minimizes the integrity risk. The proposed algorithm is not as computationally efficient as the method given in [12], but it generates tighter bounds on integrity risk, and provides graphical representations that will be exploited in future work.

Finally, detailed performance analyses are carried out. When compared to a SS RAIM algorithm that uses a LS estimator, the new method demonstrates great potential to reduce the integrity risk while maintaining similar levels of accuracy.

APPENDIX I: COVARIANCE MATRIX OF THE SOLUTION SEPARATION VECTOR

This appendix proves that:

$$\mathbf{P}_\Delta = \mathbf{P}_B - \mathbf{P}$$

Let $E\{\}$ be the expected-value operator. The solution separation covariance matrix is defined as:

$$\mathbf{P}_\Delta \equiv E\{\Delta\Delta^T\} \quad (\text{A.1})$$

Substituting equation 26 for Δ into A.1 results in:

$$\mathbf{P}_\Delta = E\{(\boldsymbol{\varepsilon} - \boldsymbol{\varepsilon}_B)(\boldsymbol{\varepsilon} - \boldsymbol{\varepsilon}_B)^T\} \quad (\text{A.2})$$

The mean value of $\boldsymbol{\varepsilon}$ is implicitly removed for the covariance derivation. Equation A.2 becomes:

$$\mathbf{P}_\Delta = E\{(\mathbf{S}\mathbf{v} - \mathbf{S}_B\mathbf{v}_B)(\mathbf{S}\mathbf{v} - \mathbf{S}_B\mathbf{v}_B)^T\} \quad (\text{A.3})$$

$$\mathbf{P}_\Delta = \mathbf{S}\mathbf{V}\mathbf{S}^T - \mathbf{S}E\{\mathbf{v}\mathbf{v}_B^T\}\mathbf{S}_B^T - \mathbf{S}_B E\{\mathbf{v}_B\mathbf{v}^T\}\mathbf{S}^T + \mathbf{S}_B\mathbf{V}_B\mathbf{S}_B^T \quad (\text{A.4})$$

where $\mathbf{V} = E\{\mathbf{v}\mathbf{v}^T\}$ and $\mathbf{V}_B = E\{\mathbf{v}_B\mathbf{v}_B^T\}$

The first and last terms in equation A.4 can be written as:

$$\mathbf{S}\mathbf{V}\mathbf{S}^T = \mathbf{P}\mathbf{H}^T\mathbf{V}^{-1}\mathbf{V}\mathbf{V}^{-1}\mathbf{H}\mathbf{P} = \mathbf{P} \quad (\text{A.5})$$

similarly, $\mathbf{S}_B\mathbf{V}_B\mathbf{S}_B^T = \mathbf{P}_B \quad (\text{A.6})$

In addition, the following result is derived using the definitions in equations 11 and 12, and assuming that $E\{\mathbf{v}_A\mathbf{v}_B^T\} = \mathbf{0}$, :

$$E\{\mathbf{v}\mathbf{v}_B^T\} = E\left\{\begin{bmatrix} \mathbf{v}_A\mathbf{v}_B^T \\ \mathbf{v}_B\mathbf{v}_B^T \end{bmatrix}\right\} = \begin{bmatrix} \mathbf{0} \\ \mathbf{V}_B \end{bmatrix} \quad (\text{A.7})$$

Therefore, the second term in equation A.4 can be written as:

$$\begin{aligned} \mathbf{S}E\{\mathbf{v}\mathbf{v}_B^T\}\mathbf{S}_B^T &= \mathbf{S}\begin{bmatrix} \mathbf{0} \\ \mathbf{V}_B \end{bmatrix}\mathbf{S}_B^T \\ &= \begin{bmatrix} \mathbf{P}\mathbf{H}_A^T\mathbf{V}_A^{-1} & \mathbf{P}\mathbf{H}_B^T\mathbf{V}_B^{-1} \end{bmatrix}\begin{bmatrix} \mathbf{0} \\ \mathbf{V}_B \end{bmatrix}\mathbf{S}_B^T \quad (\text{A.8}) \\ &= \mathbf{P}\mathbf{H}_B^T\mathbf{V}_B^{-1}\mathbf{V}_B\mathbf{V}_B^{-1}\mathbf{H}_B\mathbf{P}_B = \mathbf{P} \end{aligned}$$

Similarly, the third term in equation A.4 can be written as:

$$\mathbf{S}_B \mathbf{E}\{\mathbf{v}_B \mathbf{v}_B^T\} \mathbf{S}^T = \mathbf{P} \quad (\text{A.9})$$

Substituting equations A.5, A.6, A.8 and A.9 into A.4 yields:

$$\mathbf{P}_\Delta = \mathbf{P}_B - \mathbf{P}$$

APPENDIX II: DIRECT COMPARISON OF RB AND FS RAIM TEST STATISTICS

This appendix shows that q_{RB} and q_{FS} are equivalent if and only if $n_A = n - m$.

The partition defined in equation 11 is exploited in the following derivation. The following notations are used:

$$\delta \mathbf{z} = \begin{bmatrix} \delta \mathbf{z}_A \\ \delta \mathbf{z}_B \end{bmatrix} = \begin{bmatrix} \mathbf{v}_A + \mathbf{f}_A \\ \mathbf{V}_B \end{bmatrix} \quad (\text{A.10})$$

$$\delta \mathbf{z} = \mathbf{A} \delta \mathbf{z}_A + \mathbf{B} \delta \mathbf{z}_B \quad \text{with} \quad \mathbf{B} \equiv \begin{bmatrix} \mathbf{0} \\ \mathbf{I}_{n-n_A} \end{bmatrix} \quad (\text{A.11})$$

\mathbf{A} was defined in equation 42. Substituting these notations into the residual vector and weighted norm definitions in equations 21 and 22, the RB test statistic can be expressed as:

$$q_{RB} = q_{R,A} + 2 q_{R,AB} + q_{R,B} \quad (\text{A.12})$$

where

$$\begin{aligned} q_{R,A} &= \delta \mathbf{z}_A^T \mathbf{A}^T \mathbf{V}^{-1} (\mathbf{I} - \mathbf{H}\mathbf{S}) \mathbf{A} \delta \mathbf{z}_A \\ q_{R,AB} &= \delta \mathbf{z}_A^T \mathbf{A}^T \mathbf{V}^{-1} (\mathbf{I} - \mathbf{H}\mathbf{S}) \mathbf{B} \delta \mathbf{z}_B \\ q_{R,B} &= \delta \mathbf{z}_B^T \mathbf{B}^T \mathbf{V}^{-1} (\mathbf{I} - \mathbf{H}\mathbf{S}) \mathbf{B} \delta \mathbf{z}_B \end{aligned}$$

It is worth noticing that [24]:

$$\mathbf{V}^{-1} (\mathbf{I} - \mathbf{H}\mathbf{S}) = (\mathbf{I} - \mathbf{H}\mathbf{S})^T \mathbf{V}^{-1} (\mathbf{I} - \mathbf{H}\mathbf{S})$$

Similarly, substituting the partitioned measurement error notations into the definitions of the solution separation vector and of its weighted norm in equations 26 and 32, the FS test statistic can be expressed by as:

$$q_{FS} = q_{S,A} + 2 q_{S,AB} + q_{S,B} \quad (\text{A.13})$$

where,

$$\begin{aligned} q_{S,A} &= \delta \mathbf{z}_A^T \mathbf{A}^T \mathbf{S}^T \mathbf{P}_\Delta^+ \mathbf{S} \mathbf{A} \delta \mathbf{z}_A \\ q_{S,AB} &= \delta \mathbf{z}_A^T \mathbf{A}^T \mathbf{S}^T \mathbf{P}_\Delta^+ \mathbf{S}_\Delta \mathbf{B} \delta \mathbf{z}_B \end{aligned}$$

$$q_{S,B} = \delta \mathbf{z}_B^T \mathbf{B}^T \mathbf{S}_\Delta^T \mathbf{P}_\Delta^+ \mathbf{S}_\Delta \mathbf{B} \delta \mathbf{z}_B$$

Equation 43 was used to obtain the above expressions of $q_{S,A}$ and $q_{S,AB}$.

This appendix is organized in three steps that will show that:

$$q_{S,A} = q_{R,A}, \quad q_{S,AB} = q_{R,AB}$$

but, $q_{S,B} = q_{R,B}$ if only if $n_A = n - m$

A. Step 1: $q_{S,A} = q_{R,A}$

First, it is shown that $q_{S,A} = q_{R,A}$. Using the matrix pseudo-inversion identity in Appendix IV, $q_{S,A}$ can be rewritten as:

$$q_{S,A} = \delta \mathbf{z}_A^T \mathbf{A}^T \mathbf{S}^T (-\mathbf{P}^{-1} (\mathbf{P}_B^{-1} - \mathbf{P}^{-1}) + \mathbf{P}^{-1} - \mathbf{P}^{-1}) \mathbf{S} \mathbf{A} \delta \mathbf{z}_A \quad (\text{A.14})$$

It can easily be shown by substituting the definitions of the partitioning of \mathbf{H} and \mathbf{V} (in equations 11 and 12) into 13, that:

$$\mathbf{P}^{-1} = \mathbf{P}_B^{-1} + \mathbf{H}_A^T \mathbf{V}_A^{-1} \mathbf{H}_A \quad (\text{A.15})$$

Using the definition of \mathbf{S} in equation 14, equation A.14 is rewritten as:

$$q_{S,A} = \delta \mathbf{z}_A^T \mathbf{C} \delta \mathbf{z}_A - \delta \mathbf{z}_A^T \mathbf{V}_A^{-1} \mathbf{H}_A \mathbf{P} \mathbf{H}_A^T \mathbf{V}_A^{-1} \delta \mathbf{z}_A \quad (\text{A.16})$$

where $\mathbf{C} \equiv \mathbf{V}_A^{-1} \mathbf{H}_A (\mathbf{H}_A^T \mathbf{V}_A^{-1} \mathbf{H}_A)^+ \mathbf{H}_A^T \mathbf{V}_A^{-1}$ (A.17)

Pre-multiplying \mathbf{C} by \mathbf{H}_A^T and post-multiplying it by \mathbf{H}_A yields:

$$\mathbf{H}_A^T \mathbf{C} \mathbf{H}_A = \mathbf{H}_A^T \mathbf{V}_A^{-1} \mathbf{H}_A (\mathbf{H}_A^T \mathbf{V}_A^{-1} \mathbf{H}_A)^+ \mathbf{H}_A^T \mathbf{V}_A^{-1} \mathbf{H}_A \quad (\text{A.18})$$

Using the definition of the Moore-Penrose pseudo-inverse in equation 29, the following result is obtained:

$$\mathbf{H}_A^T \mathbf{C} \mathbf{H}_A = \mathbf{H}_A^T \mathbf{V}_A^{-1} \mathbf{H}_A \quad (\text{A.19})$$

therefore: $\mathbf{C} = \mathbf{V}_A^{-1}$ (A.20)

Substituting equation A.20 back into A.16 yields:

$$q_{S,A} = \delta \mathbf{z}_A^T \mathbf{V}_A^{-1} (\mathbf{I} - \mathbf{H}_A \mathbf{P} \mathbf{H}_A^T \mathbf{V}_A^{-1}) \delta \mathbf{z}_A \quad (\text{A.21})$$

Finally, equation A.21 shows that

$$q_{S,AB} = \delta \mathbf{z}_A^T \mathbf{A}^T \mathbf{V}^{-1} (\mathbf{I} - \mathbf{H}\mathbf{S}) \mathbf{A} \delta \mathbf{z}_A = q_{R,A} \quad (\text{A.26})$$

$$q_{S,A} = \delta \mathbf{z}_A^T \mathbf{A}^T \mathbf{V}^{-1} (\mathbf{I} - \mathbf{H}\mathbf{S}) \mathbf{A} \delta \mathbf{z}_A = q_{R,A}$$

B. Step 2: $q_{S,AB} = q_{R,AB}$

The proof is similar to that of Step 1. The following result is used:

$$\mathbf{S}_\Delta \mathbf{B} = \mathbf{S}\mathbf{B} - \mathbf{S}_B \quad (\text{A.22})$$

which is obvious from the definition of \mathbf{S}_Δ and \mathbf{B} in equations 27 and A.11. Thus, the scalar $q_{S,AB}$ is expressed as:

$$q_{S,AB} = \delta \mathbf{z}_A^T \mathbf{A}^T \mathbf{S}^T \mathbf{P}_\Delta^+ (\mathbf{S}\mathbf{B} - \mathbf{S}_B) \delta \mathbf{z}_B \quad (\text{A.23})$$

Using again the matrix pseudo-inversion identity, equation A.23 becomes:

$$q_{S,AB} = \delta \mathbf{z}_A^T \mathbf{A}^T \mathbf{S}^T (\mathbf{P}^{-1} (\mathbf{H}_A^T \mathbf{V}_A^{-1} \mathbf{H}_A)^+ \mathbf{P}^{-1} - \mathbf{P}^{-1}) (\mathbf{S}\mathbf{B} - \mathbf{S}_B) \delta \mathbf{z}_B$$

The following equations are then substituted into that last expression:

$$\mathbf{S}\mathbf{A} = \mathbf{P}\mathbf{H}_A^T \mathbf{V}_A^{-1}, \quad \mathbf{S}\mathbf{B} = \mathbf{P}\mathbf{H}_B^T \mathbf{V}_B^{-1}$$

which yields:

$$q_{S,AB} = \delta \mathbf{z}_A^T \mathbf{D} \delta \mathbf{z}_B - \delta \mathbf{z}_A^T \mathbf{V}_A^{-1} \mathbf{H}_A \mathbf{P} \mathbf{H}_B^T \mathbf{V}_B^{-1} \delta \mathbf{z}_B \quad (\text{A.24})$$

where

$$\mathbf{D} \equiv \mathbf{V}_A^{-1} \mathbf{H}_A (\mathbf{H}_A^T \mathbf{V}_A^{-1} \mathbf{H}_A)^+ \mathbf{H}_B^T \mathbf{V}_B^{-1} - \mathbf{V}_A^{-1} \mathbf{H}_A (\mathbf{H}_A^T \mathbf{V}_A^{-1} \mathbf{H}_A)^+ \mathbf{P}^{-1} \mathbf{S}_B + \mathbf{V}_A^{-1} \mathbf{H}_A \mathbf{S}_B$$

Pre-multiplying \mathbf{D} by $\mathbf{H}_A^T \mathbf{V}_A^{-1}$, post-multiplying it by $\mathbf{H}_A^T \mathbf{V}_A^{-1} \mathbf{H}_A$, using equation A.15 and the definition of the Moore Penrose pseudo-inverse in equation 29, the following result is obtained:

$$\mathbf{D} = \mathbf{H}_A^T \mathbf{V}_A^{-1} \mathbf{H}_A + \left[-\mathbf{P}_B - \mathbf{H}_A^T \mathbf{V}_A^{-1} \mathbf{H}_A (\mathbf{H}_A^T \mathbf{V}_A^{-1} \mathbf{H}_A)^+ + \mathbf{P}_B \right] \mathbf{H}_A^T \mathbf{V}_A^{-1} \mathbf{H}_A$$

Using again equation 29, it is shown that:

$$\mathbf{D} = \mathbf{0} \quad (\text{A.25})$$

Finally, substituting equation A.25 into A.24 provides the following result:

C. Step 3: $q_{S,B} = q_{R,B}$ if only if $n_A = n - m$

This result is simpler to prove because the following simplification can be made:

$$\mathbf{S}_\Delta \mathbf{B} = \mathbf{S}\mathbf{B} - \mathbf{S}_B = ((\mathbf{P} - \mathbf{P}_B) \mathbf{H}_B^T \mathbf{V}_B^{-1}) = -\mathbf{P}_\Delta \mathbf{H}_B^T \mathbf{V}_B^{-1}$$

Substituting this result into the expression of $q_{S,B}$ in equation A.13 yields:

$$q_{S,B} = \delta \mathbf{z}_B^T \mathbf{V}_B^{-1} \mathbf{H}_B \mathbf{P}_\Delta \mathbf{H}_B^T \mathbf{V}_B^{-1} \delta \mathbf{z}_B \quad (\text{A.27})$$

Substituting equation 28 into A.27 results in:

$$q_{S,B} = \delta \mathbf{z}_B^T \mathbf{V}_B^{-1} \mathbf{H}_B (\mathbf{P}_B - \mathbf{P}) \mathbf{H}_B^T \mathbf{V}_B^{-1} \delta \mathbf{z}_B$$

Simplifying this last expression provides the following equation:

$$q_{S,B} = \delta \mathbf{z}_B^T \mathbf{V}_B^{-1} (\mathbf{H}_B \mathbf{S}_B - \mathbf{H}_B \mathbf{P} \mathbf{H}_B^T \mathbf{V}_B^{-1}) \delta \mathbf{z}_B \quad (\text{A.28})$$

Recall that $q_{R,B}$ in equation A.12 is expressed as:

$$q_{R,B} = \delta \mathbf{z}_B^T \mathbf{V}_B^{-1} (\mathbf{I} - \mathbf{H}_B \mathbf{P} \mathbf{H}_B^T \mathbf{V}_B^{-1}) \delta \mathbf{z}_B$$

Equation A.28 can only be equivalent to $q_{R,B}$ if \mathbf{S}_B , which is the left pseudo inverse of \mathbf{H}_B is also the right pseudo-inverse of \mathbf{H}_B . Therefore, \mathbf{S}_B should be the inverse of the $n - n_A \times m$ matrix \mathbf{H}_B , which is only possible if \mathbf{H}_B is a square matrix. Hence the condition for $q_{R,B}$ and $q_{S,B}$ to be identical is that:

$$n - n_A = m$$

which is the same as: $n_A = n - m$

If this condition is fulfilled, then it is true that:

$$q_{S,B} = q_{R,B}$$

D. Conclusion of the Appendix:

Equality between RB and FS test statistics ($q_{RB} = q_{FS}$) is proved if and only if:

$$n_A = n - m$$

APPENDIX III: DIRECT COMPARISON OF RB AND SS RAIM TEST STATISTICS

This appendix shows that

$$q_{RB} = q_{SS} \quad \text{if and only if} \quad n_A = n - m = 1$$

Recall equation A.15:

$$\mathbf{P}_B^{-1} = \mathbf{P}^{-1} - \mathbf{H}_A^T \mathbf{V}_A^{-1} \mathbf{H}_A$$

The variance of the fault-free subset solution can be expressed as:

$$\begin{aligned} \sigma_B^2 &= \mathbf{a}^T \mathbf{P}_B \mathbf{a} \\ &= \mathbf{a}^T \left(\mathbf{P}^{-1} - \mathbf{H}_A^T \mathbf{V}_A^{-1} \mathbf{H}_A \right) \mathbf{a} \\ &= \mathbf{a}^T \left(\mathbf{P}^{-1} - \mathbf{H}_A^T \mathbf{V}_A^{-1} \mathbf{V}_A \mathbf{V}_A^{-1} \mathbf{H}_A \right) \mathbf{a} \end{aligned} \quad (\text{A.29})$$

Using the matrix inversion identity (also known as Woodbury's formula), equation A.29 becomes:

$$\begin{aligned} \sigma_B^2 &= \mathbf{a}^T \left(\mathbf{P} + \mathbf{P} \mathbf{H}_A^T \mathbf{V}_A^{-1} \left(\mathbf{V}_A^{-1} - \mathbf{V}_A^{-1} \mathbf{H}_A \mathbf{P} \mathbf{H}_A^T \mathbf{V}_A^{-1} \right)^{-1} \mathbf{V}_A^{-1} \mathbf{H}_A \mathbf{P} \right) \mathbf{a} \\ &= \sigma^2 + \mathbf{a}^T \mathbf{P} \mathbf{H}_A^T \mathbf{V}_A^{-1} \left(\mathbf{V}_A^{-1} - \mathbf{V}_A^{-1} \mathbf{H}_A \mathbf{P} \mathbf{H}_A^T \mathbf{V}_A^{-1} \right)^{-1} \mathbf{V}_A^{-1} \mathbf{H}_A \mathbf{P} \mathbf{a} \\ &= \sigma^2 + \mathbf{s}^T \mathbf{A} \left(\mathbf{A}^T \mathbf{V} (\mathbf{I} - \mathbf{H} \mathbf{S}) \mathbf{A} \right)^{-1} \mathbf{A}^T \mathbf{s} \end{aligned}$$

An expression of the variance of the single-state solution separation is obtained:

$$\sigma_\Delta^2 = \sigma_B^2 - \sigma^2 = \mathbf{s}^T \mathbf{A} \left(\mathbf{A}^T \mathbf{V} (\mathbf{I} - \mathbf{H} \mathbf{S}) \mathbf{A} \right)^{-1} \mathbf{A}^T \mathbf{s} \quad (\text{A.30})$$

Pre-multiplying both sides by $\mathbf{A}^T \mathbf{s}$ and post-multiplying by $\mathbf{s}^T \mathbf{A}$ yields:

$$\sigma_\Delta^2 \mathbf{A}^T \mathbf{s} \mathbf{s}^T \mathbf{A} = \mathbf{A}^T \mathbf{s} \mathbf{s}^T \mathbf{A} \left(\mathbf{A}^T \mathbf{V} (\mathbf{I} - \mathbf{H} \mathbf{S}) \mathbf{A} \right)^{-1} \mathbf{A}^T \mathbf{s} \mathbf{s}^T \mathbf{A}$$

In the case where $n_A = 1$, $\mathbf{A}^T \mathbf{s} \mathbf{s}^T \mathbf{A}$ is a non-zero scalar. Multiplying both sides of the previous equation by the inverse squared of this scalar and taking the inverse of the entire equation gives the following equation:

$$\mathbf{A}^T \mathbf{s} \mathbf{s}^T \mathbf{A} / \sigma_\Delta^2 = \mathbf{A}^T \mathbf{V}^{-1} (\mathbf{I} - \mathbf{H} \mathbf{S}) \mathbf{A} \quad (\text{A.31})$$

Finally, by definition in equations 24 and 40, the non-centrality parameters of q_{RB} and q_{SS} can respectively be expressed as:

$$\lambda_{RB}^2 = \mathbf{f}_A^T \mathbf{A}^T \mathbf{V}^{-1} (\mathbf{I} - \mathbf{H} \mathbf{S}) \mathbf{A} \mathbf{f}_A \quad (\text{A.32})$$

$$\lambda_{SS}^2 = \mathbf{f}_A^T \mathbf{A}^T \mathbf{s} \mathbf{s}^T \mathbf{A} \mathbf{f}_A / \sigma_\Delta^2 \quad (\text{A.33})$$

Therefore, equation A.31 shows that, if $n_A = 1$, then

$$\lambda_{RB}^2 = \lambda_{SS}^2 \quad (\text{A.34})$$

This result has also been demonstrated (in a slightly different form, and using different methods) in [9] and [21]. Interestingly, even though λ_{SS}^2 is a function of \mathbf{a} and σ_Δ^2 , it is actually independent of the state of interest (since it is equal to λ_{RB}^2).

Finally, q_{RB} and q_{SS} are both equivalent, i.e., non-centrally chi-square distributed with the same non-centrality parameter (equation A.34), and with 1 degree of freedom if and only if $n - m = 1$ (as shown in equations 23 and 39). Therefore, it is true that:

$$q_{RB} = q_{SS} \quad \text{if and only if} \quad n_A = n - m = 1$$

APPENDIX IV: PROOF OF A MATRIX PSEUDOINVERSION IDENTITY

In this appendix, it is shown that:

$$\mathbf{H}_A \mathbf{P} \mathbf{P}_\Delta^+ \mathbf{P} \mathbf{H}_A^T = \mathbf{H}_A \mathbf{P} \left(-\mathbf{P}^{-1} - \mathbf{P}^{-1} (\mathbf{P}_B^{-1} - \mathbf{P}^{-1})^+ \mathbf{P}^{-1} \right) \mathbf{P} \mathbf{H}_A^T$$

which, by substituting the expression of $\mathbf{P}_B^{-1} - \mathbf{P}^{-1}$ in equation A.15, becomes:

$$\mathbf{H}_A \mathbf{P} \mathbf{P}_\Delta^+ \mathbf{P} \mathbf{H}_A^T = \mathbf{H}_A \mathbf{P} \left(-\mathbf{P}^{-1} + \mathbf{P}^{-1} (\mathbf{H}_A^T \mathbf{V}_A^{-1} \mathbf{H}_A)^+ \mathbf{P}^{-1} \right) \mathbf{P} \mathbf{H}_A^T$$

Rewriting and rearranging the previous equation will show that the identity is true. First, pre-multiplying both sides of this equation by $\mathbf{H}_A^T \mathbf{V}_A^{-1}$ and post-multiplying them by $\mathbf{V}_A^{-1} \mathbf{H}_A$ provides the following equation:

$$\mathbf{P}_A^* \mathbf{P} \mathbf{P}_\Delta^+ \mathbf{P} \mathbf{P}_A^* = \mathbf{P}_A^* \mathbf{P} \left(-\mathbf{P}^{-1} + \mathbf{P}^{-1} (\mathbf{P}_A^*)^+ \mathbf{P}^{-1} \right) \mathbf{P} \mathbf{P}_A^* \quad (\text{A.35})$$

where

$$\mathbf{P}_A^* \equiv \mathbf{H}_A^T \mathbf{V}_A^{-1} \mathbf{H}_A$$

Expanding terms, and using the definition of the Moore Penrose pseudo-inverse in equation 29, equation A.35 becomes:

$$\mathbf{P}_A^* \mathbf{P} \mathbf{P}_\Delta^+ \mathbf{P} \mathbf{P}_A^* = -\mathbf{P}_A^* \mathbf{P} \mathbf{P}_A^* + \mathbf{P}_A^* \quad (\text{A.36})$$

Substituting equation A.15 for all \mathbf{P}_A^* -terms (i.e., $\mathbf{P}_A^* = \mathbf{P}^{-1} - \mathbf{P}_B^{-1}$), expanding the resulting expression, and simplifying yields:

$$\mathbf{P}_B \mathbf{P}_\Delta^+ \mathbf{P}_B + \mathbf{P} \mathbf{P}_\Delta^+ \mathbf{P} - \mathbf{P} \mathbf{P}_\Delta^+ \mathbf{P}_B - \mathbf{P}_B \mathbf{P}_\Delta^+ \mathbf{P} = -\mathbf{P} + \mathbf{P}_B \quad (\text{A.37})$$

The right hand side turns out to be \mathbf{P}_Δ (equation 28 is $\mathbf{P}_\Delta = \mathbf{P}_B - \mathbf{P}$). Using again the definition of the Moore Penrose pseudo inverse to rewrite the right hand side term, and arranging terms on the left hand side, equation A.37 becomes:

$$(\mathbf{P}_B - \mathbf{P}) \mathbf{P}_\Delta^+ (\mathbf{P}_B - \mathbf{P}) = \mathbf{P}_\Delta \mathbf{P}_\Delta^+ \mathbf{P}_\Delta$$

Finally, using equation 28 again, it becomes obvious that the matrix pseudo-inversion identity is true.

APPENDIX V: INDEPENDENCE OF RB, FS AND SS TEST STATISTICS FROM LEAST-SQUARES ESTIMATE ERRORS

A. Independence of RB Test Statistic and Least-Squares Estimate Error

It has been shown in [7, 20] that the random parts of the least-squares (LS) estimate error vector $\boldsymbol{\varepsilon}$ and of the residual vector \mathbf{r} are derived from orthogonal components of the measurement noise. $\boldsymbol{\varepsilon}$ and \mathbf{r} are also jointly normally distributed. Therefore, all elements of \mathbf{r} are linearly independent from any element of $\boldsymbol{\varepsilon}$, which ensures that the weighted norm q_{RB} of \mathbf{r} is statistically independent from the estimate error ε for the state of interest.

B. Independence of FS and SS Test Statistics from Least-Squares Estimate Error

This appendix proves the independence of the LS estimate error $\boldsymbol{\varepsilon}$ with the FS and SS test statistics q_{FS} and q_{SS} . The LS estimate error vector $\boldsymbol{\varepsilon}$ and the fault-free estimate error vector $\boldsymbol{\varepsilon}_B$ defined in equations 15 and 18 can be rewritten using the notations of equation A.11 as:

$$\boldsymbol{\varepsilon} = \mathbf{P} \mathbf{H}_A^T \mathbf{V}_A^{-1} \delta \mathbf{z}_A + \mathbf{P} \mathbf{H}_B^T \mathbf{V}_B^{-1} \delta \mathbf{z}_B \quad (\text{A.38})$$

$$\boldsymbol{\varepsilon}_B = \mathbf{P}_B \mathbf{H}_B^T \mathbf{V}_B^{-1} \delta \mathbf{z}_B \quad (\text{A.39})$$

Mean errors have no impact on this discussion about independence, therefore, within this section, it is assumed that $\mathbf{f}_A = \mathbf{0}$. The correlation matrix between $\boldsymbol{\varepsilon}$ and the full-state solution separation vector $\boldsymbol{\Delta}$ (defined in equation 26) is given by:

$$\mathbb{E}\{(\boldsymbol{\varepsilon} - \boldsymbol{\varepsilon}_B) \boldsymbol{\varepsilon}^T\} = \mathbb{E}\{\boldsymbol{\varepsilon} \boldsymbol{\varepsilon}^T\} - \mathbb{E}\{\boldsymbol{\varepsilon}_B \boldsymbol{\varepsilon}^T\} \quad (\text{A.40})$$

Substituting equations A.38 and A.39 into A.40 and recalling the following assumptions:

$$\mathbb{E}\{\mathbf{v}_A \mathbf{v}_B^T\} = \mathbf{0} \quad \text{and} \quad \mathbb{E}\{\mathbf{v}_B \mathbf{v}_B^T\} = \mathbf{V}_B$$

equation A.40 becomes:

$$\mathbb{E}\{(\boldsymbol{\varepsilon} - \boldsymbol{\varepsilon}_B) \boldsymbol{\varepsilon}^T\} = \mathbf{P} - \mathbf{P}_B \mathbf{H}_B^T \mathbf{V}_B^{-1} \mathbf{H}_B \mathbf{P}$$

Finally, using the definition of \mathbf{P}_B in equation 16, it becomes evident that:

$$\mathbb{E}\{(\boldsymbol{\varepsilon} - \boldsymbol{\varepsilon}_B) \boldsymbol{\varepsilon}^T\} = \mathbf{P} - \mathbf{P} = \mathbf{0} \quad (\text{A.41})$$

Equation A.41 shows that vectors $\boldsymbol{\varepsilon}$ and $\boldsymbol{\Delta}$ are uncorrelated. They are also jointly normally distributed. Therefore, all elements of $\boldsymbol{\Delta}$ are linearly independent from any element of $\boldsymbol{\varepsilon}$, which ensures that the weighted norms q_{FS} and q_{SS} of $\boldsymbol{\Delta}$ are statistically independent from the estimate error $\boldsymbol{\varepsilon}$ for the state of interest.

C. Generalization to Other Test Statistics

It is desirable in navigation applications to use ‘unbiased’ estimators, whose estimate errors are not a function of state vector \mathbf{x} . Let \mathbf{E} be a general unbiased estimator matrix (to be defined). The estimate error can be defined as:

$$\delta \mathbf{x} = \hat{\mathbf{x}} - \mathbf{x} = \mathbf{E} \mathbf{z} - \mathbf{x} = \mathbf{E}(\mathbf{v} + \mathbf{f})$$

The ‘unbiased’ constraint can be expressed as:

$$\mathbf{E} \mathbf{H} = \mathbf{I} \quad (\text{A.42})$$

In parallel, let \mathbf{D} be a $n_D \times 1$ detector matrix, which is voluntarily left undefined. \mathbf{D} could be the RB, FS or SS detector matrix, in which cases n_D would be equal to n , m or 1, respectively. The detector aims at observing the fault vector, and should not be a function of \mathbf{x} . The $n_D \times 1$ detector vector \mathbf{q} which would serve as basis to define a test statistic can be expressed as:

$$\mathbf{q} = \mathbf{D} \mathbf{z} = \mathbf{D}(\mathbf{v} + \mathbf{f}) \quad (\text{A.43})$$

Equation A.43 assumes that the following equation is satisfied:

$$\mathbf{D} \mathbf{H} = \mathbf{0} \quad (\text{A.44})$$

which means that \mathbf{D} maps the measurement vector into the parity space (or null space of \mathbf{H}^T). The correlation matrix between $\delta\mathbf{x}$ and \mathbf{q} is defined as (the fault vector \mathbf{f} is implicitly removed for this discussion):

$$E\{\delta\mathbf{x}\mathbf{q}^T\} = \mathbf{EVD}^T$$

Using a least squares estimator

$$E\{\delta\mathbf{x}\mathbf{q}^T\} = \mathbf{PH}^T\mathbf{V}^{-1}\mathbf{VD}^T$$

$$E\{\delta\mathbf{x}\mathbf{q}^T\} = \mathbf{PH}^T\mathbf{D}^T$$

Substituting equation A.44 into that last expression yields:

$$E\{\delta\mathbf{x}\mathbf{q}^T\} = \mathbf{0} \quad (\text{A.45})$$

Equation A.45 shows that any test statistic derived from vectors laying in the parity space are statistically independent from the LS estimate error. This will no longer be the case using non-LS estimators.

It can finally be noticed that the RB, FS, and SS detector matrices all map the measurements in the parity space, i.e.:

$$(\mathbf{I} - \mathbf{HS})\mathbf{H} = \mathbf{0}, \quad \mathbf{S}_\Delta\mathbf{H} = \mathbf{0}, \quad \text{and} \quad \mathbf{s}_\Delta^T\mathbf{H} = \mathbf{0} \quad (\text{A.46})$$

APPENDIX VI: COMPARISONS OF NON-CENTRALITY PARAMETERS FOR RB, FS AND SS TEST STATISTICS

A. Comparison of RB versus FS Test Statistics

Appendix II-A provides a proof of the following equation:

$$q_{R,A} = q_{S,A}$$

and therefore, it also proves that $\lambda_{RB} = \lambda_{FS}$, which remains true for the worst case fault vector $\bar{\mathbf{f}}$, so that:

$$\bar{\lambda}_{RB}^2 = \bar{\lambda}_{FS}^2$$

It also means that, since both methods use the same estimator, $\bar{\mathbf{f}}$ for RB and FS RAIM is identical, and so is the worst-case slope \bar{g}_F . The worst-case slope squared is derived in equation 50, and for the RB method is:

$$\bar{g}_F^2 = \mathbf{s}^T \mathbf{A} \mathbf{A}^T \mathbf{V}^{-1} (\mathbf{I} - \mathbf{HS})^{-1} \mathbf{A} \mathbf{A}^T \mathbf{s} \quad (\text{A.46})$$

It turns out that the term in the right hand side of equation A.46 has already appeared in a previous equation A.30. It implies the following equation:

$$\bar{g}_F^2 = \mathbf{s}^T \mathbf{A} (\mathbf{A}^T \mathbf{V} (\mathbf{I} - \mathbf{HS}) \mathbf{A})^{-1} \mathbf{A}^T \mathbf{s} = \sigma_\Delta^2 \quad (\text{A.47})$$

B. Comparison of RB versus SS Test Statistics

The worst-case slope squared is derived in equation 50, and for SS RAIM, it can be expressed as:

$$\bar{g}_F^2 = \mathbf{s}^T \mathbf{A} (\mathbf{A}^T \mathbf{s} \mathbf{s}^T \mathbf{A} / \sigma_\Delta^2)^{\dagger} \mathbf{A}^T \mathbf{s} \quad (\text{A.48})$$

Dividing both sides of A.48 by σ_Δ^2 yields an interesting result:

$$\bar{g}_F^2 / \sigma_\Delta^2 = \mathbf{s}^T \mathbf{A} (\mathbf{A}^T \mathbf{s} \mathbf{s}^T \mathbf{A})^{\dagger} \mathbf{A}^T \mathbf{s}$$

$\bar{g}_F^2 / \sigma_\Delta^2$ is symmetric (by definition of the Moore Penrose pseudo-inverse in equation 29), and again using equation 29, it can be seen that it is idempotent. In addition, $\bar{g}_F^2 / \sigma_\Delta^2$ is a scalar. Therefore, its value must be one. It follows that:

$$\bar{g}_F^2 = \sigma_\Delta^2 \quad (\text{A.49})$$

Equations A.49 and A.47 prove that the worst case slope \bar{g}_F is the same for all three RAIM methods, and that it is equal to σ_Δ .

C. Generalization to Other Test Statistics in the Case of Single-SV Faults

The first step of this generalization is a change of variable to normalize the measurement vector \mathbf{z} in 8:

$$\mathbf{z}_* = \mathbf{H}_* \mathbf{x} + \delta\mathbf{z}_* \quad (\text{A.50})$$

where:

$$\mathbf{z}_* = \mathbf{V}^{-1/2} \mathbf{z} \quad (\text{A.51})$$

$$\mathbf{H}_* = \mathbf{V}^{-1/2} \mathbf{H} \quad \text{and} \quad \delta\mathbf{z}_* = \mathbf{V}^{-1/2} \delta\mathbf{z} \quad (\text{A.52})$$

The resulting measurement error distribution is given by:

$$\delta\mathbf{z}_* \sim \mathcal{N}(\mathbf{0}, \mathbf{I}),$$

Consider a detector defined in a similar manner as in Appendix V-C. The choice is made to design the

detector's test statistic (square rooted) as a linear combination of the parity vector:

$$q^{1/2} = \mathbf{u}^T \mathbf{Q}_* \mathbf{z}_* = \mathbf{u}^T \mathbf{Q}_* \delta \mathbf{z}_* \quad (\text{A.53})$$

where \mathbf{Q}_* is the $(n-m) \times n$ parity matrix (e.g., defined in [7]), \mathbf{u} is a $(n-m) \times 1$ unit vector, whose direction must be determined. By definition, \mathbf{Q}_* satisfies the following equations:

$$\mathbf{Q}_* \mathbf{H} = \mathbf{0} \quad \text{and} \quad \mathbf{Q}_* \mathbf{Q}_*^T = \mathbf{I} \quad (\text{A.51})$$

Vector \mathbf{u} is defined as unit-norm to avoid further normalization step when computing the test statistic q . The detector matrix $\mathbf{u}^T \mathbf{Q}_*$ satisfies equation A.44. In this case, the worst-case fault slope can be expressed using equation 50 as:

$$\bar{g}_F^2 = \mathbf{s}^T \mathbf{A} (\mathbf{A}^T \mathbf{Q}_*^T \mathbf{u} \mathbf{u}^T \mathbf{Q}_* \mathbf{A})^+ \mathbf{A}^T \mathbf{s} \quad (\text{A.52})$$

In the case of single-satellite faults, which have the largest contribution to the integrity risk because of their higher probability of occurrence, $\mathbf{Q}_* \mathbf{A}$ is a $(n-m) \times 1$ vector. The best detector is found for the vector \mathbf{u} that minimizes the worst-case fault slope, i.e., that maximizes the matrix: $\mathbf{A}^T \mathbf{Q}_*^T \mathbf{u} \mathbf{u}^T \mathbf{Q}_* \mathbf{A}$. Therefore, for single-SV faults, vector \mathbf{u} is selected to be aligned with $\mathbf{Q}_* \mathbf{A}$, and can be expressed as:

$$\mathbf{u} = \mathbf{Q}_* \mathbf{A} / (\mathbf{A}^T \mathbf{Q}_*^T \mathbf{Q}_* \mathbf{A})^{1/2} \quad (\text{A.53})$$

Substituting A.53 into A.52 results in:

$$\bar{g}_F^2 = \mathbf{s}^T \mathbf{A} (\mathbf{A}^T \mathbf{Q}_*^T \mathbf{Q}_* \mathbf{A})^{-1} \mathbf{A}^T \mathbf{s}$$

It can be verified numerically that in this case again:

$$\bar{g}_F^2 = \sigma_\Delta^2$$

Therefore, the worst-case fault slope \bar{g}_F of a detector designed to minimize \bar{g}_F is σ_Δ . In other words, it is proved for single-SV faults, that RB, FS and SS all minimize the worst-case fault slope σ_Δ , and that their test statistics are derived from vectors that are aligned with the 'characteristic fault mode line' in the parity space.

APPENDIX VII: CONTINUITY RISK ALLOCATION

The detection thresholds for SS are defined in equation 62 as:

$$P(1FA | H_0) + P(2FA | H_0) + \dots + P(n_H FA | H_0) = P_{CONT}$$

where

- 1FA regroups the events of a single false alarm

$$\begin{aligned} P(1FA | H_0) = & P(q_1 \geq T_1, q_2 < T_2, \dots, q_{n_H} < T_{n_H} | H_0) \\ & + P(q_1 < T_1, q_2 \geq T_2, \dots, q_{n_H} < T_{n_H} | H_0) \\ & \vdots \\ & + P(q_1 < T_1, q_2 < T_2, \dots, q_{n_H} \geq T_{n_H} | H_0) \end{aligned}$$

- 2FA designates all hypotheses of two simultaneous false alarms

$$\begin{aligned} P(2FA | H_0) = & P(q_1 \geq T_1, q_2 \geq T_2, \dots, q_{n_H} < T_{n_H} | H_0) \\ & + P(q_1 < T_1, q_2 \geq T_2, q_3 \geq T_3, \dots, q_{n_H} < T_{n_H} | H_0) \\ & \vdots \\ & + P(q_1 < T_1, q_2 < T_2, \dots, q_{n_H-1} \geq T_{n_H-1}, q_{n_H} \geq T_{n_H} | H_0) \end{aligned}$$

- $n_H FA$ occurs when all thresholds are simultaneously exceeded

$$P(n_H FA | H_0) = P(q_1 \geq T_1, q_2 \geq T_2, \dots, q_{n_H} \geq T_{n_H} | H_0)$$

For simplicity, equal allocation P_{CONTi} is assumed between all n_H hypotheses. This is again a conservative assumption (also, it has been shown that optimal continuity risk requirement allocation has a small impact on the overall integrity risk [9]).

Under this additional assumption of uncorrelated q_i , the left-hand-side terms in equation 62 can be expressed, as:

$$P(1FA | H_0) = C_1^{n_H} P_{CONTi} (1 - P_{CONTi})^{n_H-1} \quad (\text{A.54})$$

$$P(2FA | H_0) = C_2^{n_H} P_{CONTi}^2 (1 - P_{CONTi})^{n_H-2} \quad (\text{A.55})$$

$$P(n_H FA | H_0) = C_{n_H}^{n_H} P_{CONTi}^{n_H} \quad (\text{A.56})$$

Equations A.54 to A.56 can be approximated because P_{CONT} (and hence P_{CONTi}) is a small number relative to 1

(P_{CONT} is lower than 10^{-5} in aircraft approach navigation). Substituting these results into equation 62 suggests the following conservative allocation:

$$\sum_{k=1}^{n_H} C_k^{n_H} P_{CONT}^k = P_{CONT} \quad (\text{A.57})$$

Rather than solving for P_{CONT} in equation A.57, higher order terms are often neglected [8, 9], so that the allocation can be taken as:

$$P_{CONT} = P_{CONT} / n_H \quad (\text{A.58})$$

APPENDIX VIII: PROTECTION LEVEL DERIVATION FOR SS RAIM

The integrity risk under a hypothesis H_i is defined as a joint probability (as in equation 7):

$$P\left(|\varepsilon| > \ell, |q_i| < T_i \mid H_i\right) \quad (\text{A.59})$$

As an alternative to evaluating the integrity risk, a protection level p_L can be derived, which is a bound on the estimate error for an integrity risk requirement allocation $I_{REQ,i}$ (which can be optimized using the method given in [9]). The formulation of the p_L equation is similar to that of the integrity risk. The protection level p_L is defined as:

$$I_{REQ,i} = P\left(|\varepsilon| > p_{L,i}, |q_i| < T_i \mid H_i\right) \quad (\text{A.60})$$

Equation (A.60) can be rewritten using conditional probabilities (without requiring the assumption of independence between ε and q_i) as:

$$I_{REQ,i} = P\left(|\varepsilon| > p_{L,i} \mid H_i, |q_i| < T_i\right) P\left(|q_i| < T_i \mid H_i\right)$$

A conservative assumption is made at this point:

The probability $P\left(|q_i| < T_i \mid H_i\right)$ is smaller than 1, and hence can be bounded by 1. The p_L is redefined as:

$$I_{REQ,i} = P\left(|\varepsilon| > p_{L,i} \mid H_i, |q_i| < T_i\right) \quad (\text{A.61})$$

Without loss of generality and for notation purposes, it is assumed that hypothesis H_i is H_A described in equation 11. Assuming $H_i \equiv H_A$, equation A.61 becomes:

$$I_{REQ,A} = P\left(|\varepsilon_B + \varepsilon - \varepsilon_B| > p_{L,A} \mid H_A, |q_{SS}| < T_{SS}\right) \quad (\text{A.62})$$

Because $\varepsilon - \varepsilon_B = q_{SS}\sigma_\Delta$, $p_{L,A}$ can be redefined again considering the worst case fault direction:

$$I_{REQ,A} = P\left(|\varepsilon_B| + |q_{SS}\sigma_\Delta| > p_{L,A} \mid H_A, |q_{SS}| < T_{SS}\right) \quad (\text{A.63})$$

Finally, a simple expression of p_L is obtained for the worst case fault magnitude:

$$p_{L,A} = Q^{-1}\{I_{REQ,A}/2\} \sigma_B + Q^{-1}\{P_{CONT}/2\} \sigma_\Delta \quad (\text{A.64})$$

where $Q^{-1}\{\}$ is the inverse tail probability distribution of the two-tailed standard normal distribution ($Q\{\} = 1 - \Phi\{\}$, where $\Phi\{\}$ is the standard normal cumulative distribution function).

REFERENCES

- [1] Walter, T., Enge, P., Blanch, J., and Pervan, B., "Worldwide Vertical Guidance of Aircraft Based on Modernized GPS and New Integrity Augmentations," Proc. of IEEE, Vol. 96, No. 12, 2008.
- [2] RTCA Special Committee 159, "Minimum Operational Performance Standards for Global Positioning System/Wide Area Augmentation System Airborne Equipment," RTCA/DO-229C, 2001, pp. 1-21.
- [3] RTCA Special Committee 159, "Minimum Aviation System Performance Standards for the Local Area Augmentation System (LAAS)," RTCA/DO-245, 2004, Appendix D. [5] Lee, Y. C., "Analysis of Range and Position Comparison Methods as a Means to Provide GPS Integrity in the User Receiver," *Proceedings of the 42nd Annual Meeting of The Institute of Navigation*, Seattle, WA, June 1986, pp. 1-4.
- [4] Lee, Y. C., "Analysis of Range and Position Comparison Methods as a Means to Provide GPS Integrity in the User Receiver," *Proceedings of the 42nd Annual Meeting of The Institute of Navigation*, Seattle, WA, 1986, pp. 1-4.
- [5] Parkinson, B. W., and Axelrad, P., "Autonomous GPS Integrity Monitoring Using the Pseudorange Residual," *NAVIGATION*, Washington, DC, Vol. 35, No. 2, 1988, pp. 225-274.

- [6] Brown, R. Grover, "A Baseline GPS RAIM Scheme and a Note on the Equivalence of Three RAIM Methods", *NAVIGATION*, Vol. 39, No. 3, Fall 1992, pp. 301-316.
- [7] Sturza, M, "Navigation System Integrity Monitoring Using Redundant Measurements," *NAVIGATION: Journal of the Institute of Navigation*, Washington, DC, Vol. 35 No. 4, 1988, pp. 69-87.
- [8] Brenner, Mats, "Integrated GPS/Inertial Fault Detection Availability," *Proceedings of the 8th International Technical Meeting of the Satellite Division of The Institute of Navigation (ION GPS 1995)*, Palm Springs, CA, September 1995, pp. 1949-1958.
- [9] Blanch, Juan, Ene, Alex, Walter, Todd, Enge, Per, "An Optimized Multiple Hypothesis RAIM Algorithm for Vertical Guidance," Proc. of ION GNSS 2007, Fort Worth, TX, September 2007, pp. 2924-2933.
- [10] Hwang, Patrick Y., Brown, R. Grover, "RAIM FDE Revisited: A New Breakthrough In Availability Performance With NIORAIM (Novel Integrity-Optimized RAIM)," Proc. of 2005 ION NTM, San Diego, CA, January 2005, pp. 654-665.
- [11] Lee, Y.C., "A New Improved RAIM Method Based on the Optimally Weighted Average Solution (OWAS) Under the Assumption of a Single Fault," Proc. of 2006 ION NTM, Monterey, CA, January 2006, pp. 574-586.
- [12] Blanch, J., Walter, T., Enge, P., "Optimal Positioning for Advanced RAIM," Proc. of ION ITM, Newport Beach, CA, January 2012, pp. 1624-1647.
- [13] Federal Aviation Administration, "Category I Local Area Augmentation System Ground Facility," *FAA-E-2937A*, 2002.
- [14] Assistant Secretary of Defense for Command, Control, Communications and Intelligence, "Global Positioning System Standard Positioning Service Performance Standard," available online at <http://www.navcen.uscg.gov/GPS/geninfo/2001SPSPerformanceStandardFINAL.pdf>, Washington, DC, 2001.
- [15] DeCleene, B., "Defining Pseudorange Integrity – Overbounding," *Proceedings of the Institute of Navigation GPS Conference*, Salt Lake City, UT., 2000, pp. 1916-1924.
- [16] Penrose, R., "A Generalized Inverse for Matrices," *Proceedings of the Cambridge Philosophical Society*, 1955, pp. 406–413.
- [17] Ben-Israel, A., and Greville, T., *Generalized Inverses*, Springer-Verlag Editor, 2003.
- [18] Angus, J. E., "RAIM with Multiple Faults", *NAVIGATION*, Vol. 53, No. 4, Winter 2006-2007, pp. 249-257.
- [19] Joergger, M., and B. Pervan. "Kalman Filter-Based Integrity Monitoring Against Sensor Faults." accepted for publication in *AIAA Journal of Guidance, Control and Dynamics*.
- [20] Pervan, B., "Navigation integrity for aircraft precision landing using the global positioning system," *Ph.D. Dissertation*, Stanford University, March 1996.
- [21] Chan, F-C., Pervan, B., "A Practical Approach to RAIM-based Fault-Tolerant Position Estimation," Proc. of ION GNSS 2010, Portland, OR, September 2010, pp. 3181-3190.
- [22] Drezner, Z., and Wesolowsky, G. O., "On the Computation of the Bivariate Normal Integral." *Journal of Statistical Computation and Simulation*. Vol. 35, 1989, pp. 101–107.
- [23] Luenberger, D. G., and Ye, Y., *Linear and Nonlinear Programming – Third Edition*, Springer Editor, 2008.
- [24] Walter, T., and Enge. P., "Weighted RAIM for Precision Approach," *Proceedings of the Institute of Navigation GPS Conference*, Palm Springs, CA, 1995.